NATIONAL ADVISORY COMMITTEE FOR AERONAUTICS

TECHNICAL NOTE 3724

CHARACTERISTICS OF FOUR NOSE INLETS AS MEASURED

AT MACH NUMBERS BETWEEN 1.4 AND 2.0

By George B. Brajnikoff and Arthur W. Rogers

Ames Aeronautical Laboratory
Moffett Field, Calif.

NACA

Washington

August 1956

NATIONAL ADVISORY COMMITTEE FOR AERONAUTICS

TECHNICAL NOTE 3724

CHARACTERISTICS OF FOUR NOSE INLETS AS MEASURED

AT MACH NUMBERS BETWEEN 1.4 AND 2.0[1]

By George B. Brajnikoff and Arthur W. Rogers

SUMMARY

The pressure recovery, mass flow, and axial force of four bodies
with nose inlets were measured at Mach numbers between 1.4 and 2.0 and
angles of attack of $0°$, $3°$, $6°$, and $9°$. The Reynolds number based on
the model inlet diameters varied between 0.4 and 0.8 million. Schlieren
photographs of models at $0°$ angle of attack were used for calculation of
the external wave drag resulting from the bow shock waves.

The drag coefficients of axially symmetric diffusers operating at
the maximum mass-flow rates were calculated from schlieren photographs
of the head shock waves and frictional drag considerations. The calcu-
lations showed good agreement with the measured values. At reduced mass-
flow ratios the agreement was only fair. The results also show that the
external drag of axially symmetric ducted bodies at $0°$ angle of attack
can be predicted to a good degree of accuracy from theoretical consider-
ations alone, if the entrance flow is supersonic and the point of tran-
sition of the boundary layer is known.

In general, it was found that the minimum axial-force coefficient
occurred with maximum mass flow through the diffuser, and a small
reduction in the mass flow resulted in a large increase in the axial-
force coefficient. At reduced mass flows the effect of mass flow on the
total-pressure recovery of a diffuser with a subsonic or a supersonic
entrance was small. Changes in the angle of attack from $0°$ to $9°$ gen-
erally caused small decreases in the total-pressure recovery. In all
cases when the maximum mass-flow decreased with increasing angle of
attack the minimum axial-force coefficient increased by a considerable
amount.

---

[1]Supersedes recently declassified NACA RM A51C12 by George B.
Brajnikoff and Arthur W. Rogers, 1951.

INTRODUCTION

The total drag of a supersonic aircraft propelled by a turbojet or a ramjet engine may be increased appreciably by an improperly designed induction system, particularly in view of the large size of the required air inlet in relation to the fuselage. Simultaneously, a low efficiency of the system in recovering the ram pressure reduces the thrust available from the engine. To avoid such consequences, a designer must be able to estimate the characteristics of inlet configurations likely to satisfy his design requirements.

For the cases of entirely supersonic flow around axially symmetric cowlings the external pressure or wave drag due to inlets can be determined theoretically (references 1 and 2). When such inlets operate at a reduced mass flow, a transonic flow region exists around the lip of the inlet and an entirely theoretical solution becomes extremely difficult. In such cases it is most practical to resort to experimental measurements of the drag force or to shadowgraph or schlieren pictures. Once the shape and location of the bow wave are known, it is possible to determine the pressure drag by the methods of references 3 and 4. A fair estimate of the frictional drag of a cowling at supersonic Mach numbers may be obtained through application of the present theories for various types of boundary layers (references 5 to 8), provided that the location of the transition region is known and there are no strong adverse pressure fields acting on the boundary layer. The pressure recovery at supersonic speeds can be estimated in cases of two-dimensional or axially symmetric inlets receiving little or no boundary layer by the methods of reference 9.

Four axially symmetric nose inlets have been tested in the Ames 8-by 8-inch supersonic wind tunnel in order to provide a basis for comparison with scoop inlets. It is the purpose of this report to present the characteristics of these nose inlets as determined by force and pressure measurements and to compare them with values calculated by various methods. Since forces were measured in the direction of the model axis only, the axial-force coefficients are presented instead of drag coefficients. Although axial and drag coefficients are synonymous only at zero angle of attack, drag symbols were used for axial forces for the sake of simplicity.

SYMBOLS

A   area, square feet

a   speed of sound, feet per second

C_a additive drag coefficient (due to diffusion ahead of entrance), dimensionless

C_D fore-drag coefficient $\left(\dfrac{D_F}{q_o A_{ref}}\right)$, dimensionless

C_{D_e} external axial-force coefficient measured along model axis $\left(\dfrac{D_e}{q_o A_{ref}}\right)$, dimensionless

C_{D_w} wave-drag coefficient $\left(\dfrac{D_e - D_f}{q_o A_{ref}}\right)$, dimensionless

D_e external force acting along model axis (does not include internal flow drag or base drag), pounds

D_F force acting along model axis (does not include base drag), pounds

D_f force acting along model axis due to friction on external model surface, pounds

d inlet diameter of cowling, feet

H total pressure, pounds per square foot

H_3 average total pressure at survey station weighted on area basis, pounds per square foot

l length of subsonic diffuser, feet

M Mach number $\left(\dfrac{V}{a}\right)$, dimensionless

m mass-flow rate $(\rho V A)$, slugs per second

m_1/m_0 mass-flow ratio (ratio of mass flowing through the diffuser to that flowing in the free stream through an area equal to that of the flow area at the inlet station, $\dfrac{\rho_1 V_1 A_1}{\rho_0 V_0 A_1}$), dimensionless

P static-pressure coefficient $\left(\dfrac{p - p_o}{q_o}\right)$, dimensionless

p static pressure, pounds per square foot

q dynamic pressure $\left(\dfrac{1}{2}\rho V^2\right)$, pounds per square foot

R body ordinate, inches

Re   Reynolds number $\left(\dfrac{Vd}{\nu}\right)$, dimensionless

V   velocity, feet per second

x   distance from inlet station along model axis, feet

α angle of attack, degrees

γ ratio of specific heats for air = 1.40, dimensionless

ν kinematic viscosity, feet squared per second

ρ mass density, slugs per cubic foot

Subscripts

o   free stream

1   inlet station

2   diffuser exit

3   settling chamber (rake station)

4   outlet station (choked flow)

base   plane surface normal to model axis and constituting the rear
boundary of the model

ref   reference area (frontal area of body exposed to stream), square
feet

APPARATUS

Wind-Tunnel and Drag Balance

The tests of this investigation were performed in the Ames 8- by
8-inch supersonic wind tunnel in the range of Mach numbers between 1.40
and 2.01. The Reynolds number per foot of length was approximately 8
million at the lowest Mach number and 11 million at the highest. A
detailed description of the tunnel and its auxiliary equipment is pre-
sented in reference 10.

Figure 1 shows the apparatus used to obtain simultaneous measure-
ments of the axial force, mass flow, and the pressure recovery of super-
sonic diffusers. As shown, a model is mounted on a steel shell that
floats on three rows of bearing balls inside a stationary shell sup-
ported by two struts. The fore and aft motion of the inner shell is
restricted only by the strain gage used for measuring axial forces.
Shrouds having somewhat smaller forward diameters than the bases of
models provide fairing between the bases of the models and the outer
shell. The shrouds and the stationary shell have orifices for measuring
static pressures acting on the base of the model and the ends of the
floating shell so that corrections for these pressures being other than
the free-stream static pressure can be made. Inside the inner shell,
which serves as a settling chamber, is a survey rake consisting of four
total and three static pressure tubes; this rake can be rotated from
outside the wind tunnel through 360° by means of a gear drive. The mass
flow through the model is controlled by a variable area outlet consist-
ing of a stationary ring and an adjustable plug operated by a wedge-
drive system. The ring is mounted rigidly on the survey-rake shaft so
that there is a clearance of 0.005 inch between its outer periphery and
the inner shell. Though such an arrangement does not allow reduction of
mass flow to zero, it provides a means for varying the flow rate without
exerting additional pressure forces on the inner shell. Measurements
with a model at angles to the stream direction can be made at angles of
3°, 6°, and 9° by attaching the balance at the proper angle in relation
to the horizontal strut as shown in figure 1.

MODEL DESCRIPTION

Figure 2 shows the models tested and gives their pertinent dimen-
sions. The first model, which was used to determine the accuracy of
force measurement, was a cone of 20° included angle; it had eight ori-
fices which were used to obtain the pressures acting on the surface of
the cone at the time of the drag-force measurement at 0° angle of attack.
The two open-nose inlet models, designated A and B, had the same external
shape. The entrance section of model A was cylindrical for a length of
1.5 diameters and was followed by a diffuser of constant divergence
angle. Model B had a contracting entrance designed so that supersonic
flow through the inlet could be established at $M_O=1.60$, according to the
relations for an inviscid, one-dimensional flow. The contraction was
followed by a short constant-area section, the purpose of which was to
stabilize a swallowed normal shock wave. This section was located so
that at a free stream Mach number of 1.70 the oblique conical-shock wave
from the cowling lip would be neutralized, if the flow were two-
dimensional, by the expansion wave originating at the forward end of the
straight section. Subsonic diffusion was accomplished by a passage of
constant divergence angle.

Model C was a conical–shock diffuser designed to handle approx–imately the same mass of air per second at a Mach number of 2.01 as the open–nose diffuser A at its maximum flow–rate condition. Model C had a 25°–semiangle cone and a cowling with a rounded lip located so that a line joining the apex of the cone and the leading edge of the cowl made a 45° angle with the model axis. The variation of the diffuser–area ratio normal to the mean–flow direction is shown in figure 3. At the design Mach number of 1.8 the diffuser was to operate with an external normal shock wave. This model was about one–eighth the size of and similar to a conical–shock diffuser tested at the NACA Lewis Laboratory in the 8– by 6–foot supersonic wind tunnel.

Model D had a 30°–semiangle cone and a cowling with a sharp lip located on a line originating at the apex of the cone and making a 46° angle with the model axis. The maximum frontal areas of models C and D were the same, but model D was designed to handle approximately 0.7 of the mass flow of model C in the test range of Mach numbers. The external surface area and length of cowling D were 55 and 62.6 percent of those of model C, respectively, and model D had steeper angles between the external surface and the model axis. The 20° cone, the central bodies (inlet cones), and the cowlings were highly polished to ensure the long–est run of laminar boundary layer possible under the existing test conditions.

TEST METHODS

Instrumentation

The tunnel total pressure, the survey–rake pressures, and the base pressures were measured on a multiple–tube mercury manometer. Dibutyl phthalate was used to measure the differences between total and static pressures registered by the survey rake at low–mass flow rates. The total temperature of the flow and the temperature of the strain gage (used for correcting the gage readings for thermal shift) were measured by thermocouples registering the temperature on an indicating potentiom–eter. Measurements of the axial force acting on the strain gage were obtained in terms of deflection of a dynamically balanced galvanometer calibrated for the gage in use. The flow about the model was observed and photographed through a schlieren apparatus having a knife edge par–allel to the direction of the free stream.

Procedure

The wind tunnel was calibrated with the aid of a rake of five static–pressure probes to determine the static–pressure gradients

existing in the test section at the nominal Mach number settings of
1.40, 1.50, 1.70, 1.90, and 2.01. During the calibration and the sub-
sequent tests, the tunnel total pressure was maintained by manual con-
trol within ±0.1 inch of mercury of the preassigned value. In general,
the test procedure was similar to that of reference 10.

The number of pressure and force readings at a fixed mass-flow rate
and different angular positions of the survey rake varied from 5 to 10,
depending on the uniformity of the total-pressure distribution in the
diffuser. The pressure recovery and the axial force were measured for
six mass-flow ratios at a given Mach number and angle of attack; the
mass-flow settings were decided upon during the test after a preliminary
observation of the rate of axial force and pressure-recovery variation
with the outlet-area changes.

Reduction of Data

The total-pressure ratio H_3/H_0, as shown on the graphs, is based
on a value of pitot pressure weighted according to area. This average
value of H_3/H_0 was used in all calculations involving total pressure.

The mass-flow ratio was calculated from the following relation:

$$\frac{m_1}{m_0} = C \left(\frac{H_3}{H_0}\right) \frac{A_4}{A_1} \frac{1}{M_0} \left(\frac{2}{\gamma+1} + \frac{\gamma-1}{\gamma+1} M_0{}^2\right)^{\frac{\gamma+1}{2(\gamma-1)}}$$

This equation was derived on the assumption that the flow was inviscid
and one-dimensional in nature; with the exception of a correction factor
C, this relation is identical to that given in reference 10. This fac-
tor was obtained by testing open-nose inlets of various inlet diameters
operating with swallowed head shock waves. The factor C was found to
be independent of small changes in the velocity profile at the survey-
rake station.

The external axial force was determined by subtracting from the
force measured by the balance the sum of the forces due to (1) the
change of momentum and static pressure of the internal flow from the free
stream to the rake station, (2) the base drag, and (3) the force due to
buoyancy. The base drag forces were caused by pressures other than the
free-stream static pressure acting on the base of the model and the
floating shell. The buoyancy force was considered to equal the inte-
grated product of the local increment in the tunnel static pressure
(existing between the local and the reference stations in the absence of
a model) and the local differential element of external surface area
normal to the model axis. Since the force normal to the model axis was
not measured, only the axial-force coefficients are presented. At 0°

angle of attack the external axial-force coefficients are equal to the external drag coefficients which include the cowl drag and drag due to diffusion ahead of the duct entrance.

Accuracy of Results

The accuracy of the test results depended principally on the time correlation as well as the precision of the pressure and force measurements since in many cases the flow through the model was unsteady. Although the force readings and the photographs of the manometer board were taken simultaneously, the difference in response of the measuring apparatus to changes in the measured quantities introduced errors of magnitudes determined by the frequency and the amplitude of the variation. The inaccuracies due to the various causes, together with their maximum cumulative magnitudes estimated in terms of the external axial-force coefficient of the model tested, are tabulated as follows:

I. Steady-flow conditions (very small and slow variation in H_o)

    A. 20° cone

        Source of error: $\pm\Delta C_{D_e}$

        1. Manometer precision and lag................... 0.002
        2. Balance friction............................. .001

           Maximum cumulative total................... 0.003

    B. Diffusers

        Source of error: $\pm\Delta C_{D_\theta}$

        1. Manometer precision and lag................... 0.002
        2. Balance friction............................. .003
        3. Internal flow momentum estimate[1]............ .003

           Maximum cumulative total.................. 0.008

II. At unsteady flow conditions the accuracy of axial-force measurements was poor.

Figure 4 shows the results of force measurements made with a 10°-semiangle cone set at 0° angle of attack. This figure also shows the theoretically predicted values of the shock-wave, or pressure, drag taken directly from the tables of reference 11 and the frictional drag as estimated on the basis of the low-speed skin-friction coefficients given

---

[1]The mass-flow ratio estimates are believed correct to ±1-1/2 percent.

in reference 5, corrected for compressibility by the method of reference 8, and modified for the three-dimensional flow effect as suggested in reference 12. All the turbulent skin-friction coefficients were corrected for compressibility using the properties of air at the model surface as suggested in reference 7. It is evident that the experimental and theoretical pressure-drag coefficients agreed very well, and that the total fore drag of the cone as measured by the balance also agreed within the expected accuracy with the predicted values of total drag based on the assumption that the boundary layer on the model was laminar. The repeatability and consistency of the results of drag-force measurements indicate that the drag balance performed satisfactorily.

RESULTS AND DISCUSSION

Open-Nose Diffusers

The variation of the total-pressure ratio and the external axial-force coefficient with mass-flow ratio of model A is shown in figure 5 for 0° angle of attack at three free-stream Mach numbers. With supersonic flow through the inlet $(m_1/m_0=1.0)$, the maximum total-pressure ratios in the settling chamber of model A were 0.93 to 0.95 of the theoretical recovery through a normal shock wave. Large transverse pressure gradients as a result of transitory separation of flow occurred in the diffuser when the area ratio between the exit and the inlet was increased more than necessary for the entrance of the normal shock wave into the inlet. This condition was manifested by the large erratic variations in the readings of the survey rake and was responsible for considerable scatter of the force data at large area ratios.

The external axial-force coefficient of model A increased rapidly at all Mach numbers with the emergence of the normal shock to a position ahead of the inlet; as the mass-flow ratio was reduced to 0.9 from 1.0, the coefficient approximately doubled in magnitude. Unfortunately, the wave drag of models A and B operating at mass-flow ratios below 1.0 could not be calculated from the schlieren pictures because the photographs did not cover a sufficiently large part of the head wave (see appendix).

At mass-flow ratios less than the maximum, the portion of the drag due to diffusion (the additive drag) can be obtained by the method of reference 13. This additive drag is accompanied by a change in the pressures on the external surface of the diffuser (reference 14). In the present tests, these pressures were not measured and the theoretical additive drag coefficients were simply added to the minimum drag coefficients. Thus, the difference between the measured and the estimated drag-rise curves is the result of neglecting the change in pressure on the cowling, of experimental and theoretical inaccuracies, and possibly

of a change in the location of the boundary—layer transition region.
However, figure 5 shows that the major portion of the drag rise can be
predicted even if these factors are ignored.

Figure 6 shows the total—pressure ratio and the external axial—
force—coefficient variation with mass—flow ratio, angle of attack, and
Mach number for model B. The maximum mass—flow ratio at the Mach number
of 1.4 was only 0.97 because the contraction of the entrance section was
too great to permit the normal shock wave to enter the inlet at that
speed or to remain inside the diffuser at $M_O = 1.4$ after entry at a
higher Mach number. The total—pressure ratio and the axial—force coef—
ficient of model B at the Mach number of 1.4 were nearly the same as
those of model A for equal mass—flow ratios. At a Mach number of 1.7
and higher, the head shock wave entered the inlet. Its position depended
entirely on the static pressure in the settling chamber of the model,
and a hysteretic variation of the total—pressure ratio with the mass—flow
ratio was observed. This is indicated in figure 6 by a peak in the
pressure—recovery curves at $m_1/m_O = 1.0$. The maximum total—pressure
ratios of model B were 0.02 to 0.04 higher than those of model A or
approximately 0.95 to 0.98 of recovery through a normal shock wave. At
equal mass—flow ratios the external axial—force coefficients of models A
and B were nearly the same.

The effects of the angle of attack on the characteristics of model
B, as shown in figure 6, were generally small. The external axial—force
coefficient seemed to increase with an increase in the angle, but the
data were inconclusive because the magnitudes of the measured effects
were comparable to experimental scatter.

Figure 7 shows the variation of the minimum external axial—force
coefficients of models A and B with Mach number at 0° angle of attack;
it also presents the values of the pressure drag, as predicted by the
method of reference 1, and the laminar and turbulent friction drag cal—
culated from the low—speed skin—friction coefficients of reference 5. A
compressibility correction to the turbulent skin—friction coefficients
has been applied as suggested in reference 7, using the properties of air
at the cowling surface. The laminar friction coefficients were corrected
for compressibility using the method of reference 8. The calculations
were made on the assumption that the frictional force on the external
surface of each model (A and B) was equal to that on a flat plate of
length and area equal to those of the cowlings.

The minimum external axial—force coefficients of model A show good
agreement with the predicted values of drag coefficients at all Mach
numbers except 2.01. A plausible explanation for the high value of the
experimental coefficient at $M_O = 2.01$ is provided by the schlieren photo—
graphs of figure 8. A mild pressure disturbance may be seen originating

on the model at a station located approximately 0.4 of the model length
from the entrance at the higher Mach number. Since this phenomenon
existed only at the highest Reynolds number, it is reasonable to assume
that it was caused by boundary—layer transition.[2] The drag coefficient
calculated on the assumption of laminar boundary layer existing on the
model up to 40 percent of the cowl length, and fully turbulent layer
from there on, agrees fairly well with the measured value. (See fig. 7.)
Better agreement would be obtained if the additional wave drag due to
the pressure disturbance were not neglected. It should be noted that
the Reynolds number based on the length of the laminar portion of the
boundary layer is quite low for natural transition (Re=1.14 million).

As shown in figure 7, the minimum external axial—force coefficient
of model B at a Mach number of 1.4 was almost one and one—half times that
of model A. The increase apparently was due to the spillage around the
cowling lip caused by the external normal shock wave. At a Mach number
of 1.5, the higher value of the minimum axial—force coefficient prevailed
when overspeeding (approaching the test Mach number from a higher value)
was not used to establish supersonic flow through the inlet. The lower
coefficient was obtained for the diffuser when the entrance velocity was
supersonic. At Mach numbers in excess of 1.5 the head shock wave entered
the diffuser without overspeeding, and the minimum axial—force coef—
ficients of model B were comparable to those of model A. Schlieren
photographs of model B reveal that at the free—stream Mach number of 2.01
transition of the boundary layer appears to have occurred at the same
location as that of model A and apparently caused a similar increase in
the measured axial—force coefficient.

Conical—Shock Diffusers

The characteristics of model C are shown in figure 9. It was found
necessary to increase the lowest test Mach number to 1.5 in order to
avoid choking the tunnel when the model was set at 9° angle of attack;
however, no difficulty was encountered at $M_0=1.4$ for $\alpha=0^o$.

The general characteristics of flow through model C were similar to
those through the open—nose diffusers with the exception that a region
of flow instability was encountered when the mass—flow ratio of model C
was reduced below about three—quarters of the maximum possible at the
given Mach number. This condition was caused possibly by the interaction

---

[2]Unpublished data of tests conducted in the NACA Ames 1— by 3—foot super—
   sonic wind tunnel and the supersonic free—flight tunnel show that mild
   pressure waves are generated by the boundary layer undergoing natural
   transition.

between the boundary layer and the shock waves on the cone and the back pressure in the subsonic diffuser (see reference 10), or by internal flow separation at the cowling wall resulting from the entrance of a velocity discontinuity sheet as suggested in reference 15.

The total-pressure recovery at the Mach number of 1.50 was 0.95 of that through a normal shock wave; at $M_O=2.01$ it was 10 percent higher than the normal wave recovery. The maximum total pressure measured in the settling chamber of this model at $M_O=1.90$ was only 3 percent less than that of the similar model tested at the Lewis Laboratory ($M_O=1.85$) at Reynolds numbers four and one-half times that of model C. These maxima occurred at the same mass-flow ratio.[8]

The values of the external axial-force coefficient at 0° angle of attack of model C were about one and a half to two times those of model A, probably because of the additive drag due to diffusion ahead of the entrance, as discussed in reference 13. Figure 9 also shows the external drag coefficients calculated from the schlieren photographs by the method of reference 3, using an approximation suggested by Nucci of the Langley Laboratory to estimate the drag due to the outer portion of the bow shock wave. (See reference 16 or appendix.) The values shown were calculated using $K=1.0$ and include the drag due to laminar friction calculated on the basis of low-speed skin-friction coefficients (reference 5) corrected for compressibility (reference 8).

In general, the assumption of laminar boundary-layer flow resulted in a fair estimate of the external drag (axial-force coefficient at $\alpha=0^O$) through the range of test Mach numbers at maximum mass-flow ratios. The drag coefficients, as calculated from wave photographs, of the inlet operating at a reduced mass flow were low in all cases. The discrepancy is probably due to the inaccuracy of calculation caused by insufficient length of the head shock wave visible in the photographs, as discussed in the appendix. At a Mach number of 2.01, where transition of the boundary layer is most likely to occur (see discussion of models A and B), and at a reduced mass-flow ratio the difference in drag coefficients amounts to that which would be caused by transition at 0.6 of the cowling length. (See fig. 9(c).) The sum of the minimum external axial-force coefficient and the additive drag coefficient, as calculated using reference 13, is also shown in figure 9. This approximation apparently gives a fair estimate of the external axial-force coefficient at moderately reduced mass-flow ratios.

---

[8] Since the mass-flow ratios as used by the Lewis Laboratory are based on the area fixed by the inlet diameter and not flow area, the numerical values of m_1/m_O are not identical unless adjusted to a common reference area.

The minimum external—axial—force coefficient of model C, as shown in figure 10, increased from 0.047 at the Mach number of 1.4 to 0.097 at $M_0=1.7$ and then decreased to 0.083 at $M_0=2.01$. This trend is consistent with that stated in reference 13 for the additive drag (which constitutes the major portion of wave drag) when the observations listed below are considered:

1. At the Mach numbers below 1.9, the normal shock wave remained outside the inlet at all mass—flow ratios.

2. At and above a Mach number of 1.9, the normal shock wave was inside the inlet at the maximum flow condition.

Figure 10 also shows the minimum external—drag or axial—force coefficients at $\alpha=0^0$ of the model tested at the Lewis Laboratory. It is evident that a fair agreement exists between the values of external wave drag coefficients of the two models after the frictional drag was subtracted. (See fig. 10.) The discrepancies may be due to the experimental inaccuracies and due to probable slight differences in the lip radii of the two cowlings. Because of the small size of model C, a small error in the lip shape due to machining may be responsible for a large portion of the observed difference in the minimum wave—drag coefficients at $M_0=2.01$. The effects of lip shape are greatest when the shape affects the position of the entrance shock wave as is the case at maximum mass—flow ratios when the free—stream Mach number is sufficiently high.

Variations in the angle of attack (see fig. 9) showed small effects on the characteristics of model C at lower Mach numbers. It should be noted that in this case the maximum mass—flow ratio was not affected appreciably. However, when the mass—flow ratio decreased 5 percent for $\alpha=9^0$ at $M_0=2.01$, the total—pressure ratio decreased approximately 6 percent and the minimum axial—force coefficient increased about 60 percent.

The characteristics of model D are presented in figure 11. The maximum mass—flow ratio of this model was larger than that of model C because of a larger cone angle, a larger angle between the model axis and the line joining the cone apex and the leading edge of the cowl, and a sharp lip. The total—pressure ratios of models D and C were nearly the same at the lower Mach numbers; at $M_0=2.01$ the maximum recovery of model D was about 5 percent greater.

The drag coefficients calculated from schlieren photographs using the same methods as those used in the case of model C also are shown in figure 11. At large mass flows the calculated drag coefficients are in fair agreement with the measured values. At all Mach numbers the

photographs showed a smaller portion of the head shock wave than with
model C, and thus the calculated values of drag were subject to greater
error. The drag coefficient (minimum plus additive) as calculated using
reference 13 seems to give a fair estimate of axial—force coefficient at
reduced mass—flow ratios.

The effects of angle of attack on the performance of model D were
large throughout the range of test Mach numbers. The largest effects on
the minimum axial—force coefficient were observed at $M_O=2.01$. For an
angle of attack change from 0° to 9°, the maximum mass—flow ratio
decreased about 8 percent and caused the minimum force coefficient to
increase approximately 20 percent and the maximum total—pressure ratio
to decrease 8 percent. The reason for the large difference in the exter-
nal axial—force coefficients at reduced mass—flow ratios (see $M_O=1.70$
curve, fig. 11) is not clearly evident.

The variation of the minimum external axial—force coefficient of
model D with the Mach number is shown in figure 12. The trend is
similar to that of model C.

In comparing the axial—force coefficients of the various models,
consideration should be given to the effects of boundary—layer transi-
tion. Transition, as indicated by schlieren photographs, is known to
have occurred on models A and B at certain test conditions. However,
this method of detecting transition is not extremely sensitive and there-
fore it is possible that transition could have occurred on the rear por-
tion of any of the models tested without being detected. Since the
frictional drag constituted a significant portion of the measured axial
force, a change in location of transition would have had a pronounced
effect on the measured force. The frictional drag was not measured
directly and, therefore, the shown variations of the external axial—
force coefficients with mass—flow ratio include the effects of changes
in the boundary layer. This fact may be responsible for at least part
of the difference between the measured values of external axial—force
coefficient at reduced mass—flow ratios and those calculated from
schlieren photographs, since the boundary layer was assumed to be
laminar.

CONCLUSIONS

The performance characteristics of four nose inlets were measured
in the NACA Ames 8— by 8—inch supersonic wind tunnel at Reynolds numbers
between 0.4 and 0.8 million based on the inlet diameters. The investi-
gation was conducted in the range of Mach numbers between 1.40 and 2.01
and led to the following conclusions:

1. Good agreement was obtained between the measured external axial-force coefficients at 0° angle of attack and the calculated drag coefficients of diffusers operating at maximum mass-flow ratios. The values of minimum wave drag obtained for a conical-shock inlet showed fair agreement with those measured in the 8- by 6-foot supersonic tunnel at the NACA Lewis Laboratory using a similar model at Reynolds numbers four and one-half times larger.

2. The external axial-force coefficients of the conical-shock inlets using all-external supersonic compression were about one and a half to two times those of the open-nose inlets with supersonic entrances.

3. Minimum external axial-force coefficients occurred at maximum mass-flow ratios and small reductions in the mass-flow ratios considerably increased the external axial-force coefficients of all the inlets.

4. The sum of the minimum external axial-force coefficients and the theoretical additive-drag coefficients gave a fair estimate of drag coefficients of inlets tested at reduced mass-flow ratios.

5. The effects of angles of attack on the pressure recovery were generally small. The external axial-force coefficients increased measurably with the angle of attack only in cases where the maximum mass-flow ratio decreased with increasing angle.

Ames Aeronautical Laboratory,
    National Advisory Committee for Aeronautics,
        Moffett Field, Calif.

APPENDIX

EVALUATION OF DRAG OF AXIALLY SYMMETRIC BODIES

FROM SHOCK—WAVE PHOTOGRAPHS

When the speed of the flow around a body changes from a supersonic velocity in the free stream to a subsonic velocity and then accelerates to a supersonic speed again, the mathematical equations that describe the flow behavior change in nature from hyperbolic to elliptic and back to hyperbolic. Since no known analytical methods exist for simultaneously solving hyperbolic and elliptic differential equations with incomplete boundary conditions, a laborious method of matching individual solutions must be used. If a photograph of the bow wave ahead of an axially sym— metric body at 0° angle of attack is available, the wave drag can be determined through use of any of the following three methods:

1. Integration of the momentum and pressure change between two infinite control planes as in figure 13

2. Integration of the entropy rise across the bow shock wave

3. Integration of the momentum and pressure change within a closed flow region adjacent to the body, the conditions within this region being calculated by the method of characteristics

These three methods have been proposed in the references cited below. It is the purpose of this appendix to review and further clarify the procedures involved by presenting derivations and detailed comments not given previously.

The first two methods require knowledge of the shape of the wave out to the point where its strength is zero, while the third method requires only the portion of the wave bounding the characteristics net ending at the rear of the body. Since in practice the entire wave cannot be photographed due to physical limitations, an approximation must be used to account for the drag contribution of the unavailable portion of the wave in the first two methods; thus the accuracy depends on the exactness with which the decay of the bow wave may be predicted.

Method 1: This method was proposed and used in reference 3. A schematic drawing of a body and its head shock wave is shown in figure 13. The body is assumed to have a blunt nose followed by an infinitely long cylindrical afterbody, so that, neglecting friction, the entire body drag appears in the detached bow wave. Considering the control

surface s shown in figure 13, one can write the following steady-flow equation for the summation of forces in the x direction on the control surface:

$$\int_s \int [\rho u V_n + p \cos (n,x)] \, ds = 0 \tag{A1}$$

where

V_n velocity compoent normal to the control surface

$p \cos (n,x)$ pressure component in the x direction

u local velocity component in the x direction

n outward normal to s

With reference to figure 13, equation (A1) may be rewritten as

$$\int_0^\infty (-\rho_0 u_0{}^2 - p_0) \, 2\pi y \, dy + \int_r^\infty (\rho u^2 + p_0) \, 2\pi \eta \, d\eta +$$

$$(\text{drag measured from } p=o) = 0$$

or

$$-2\pi \int_0^\infty (\rho_0 u_0{}^2 + p_0) \, y \, dy + 2\pi \int_r^\infty (\rho u^2 + p_0) \, \eta \, d\eta +$$

$$\int_0^r (p - p_0) \, 2\pi r_1 \, dr_1 + \int_0^r p_0 \, 2\pi r_1 \, dr_1 = 0$$

where

p local pressure on the body

Since the third integral is the body drag relative to the free-stream static pressure, the last equation may be solved for drag.

$$D_W = 2\pi \int_0^\infty (\rho_0 u_0{}^2 + p_0) \, y \, dy - 2\pi \int_r^\infty (\rho u^2 + p_0) \, \eta \, d\eta - p_0 \pi r^2$$

The second integral may be replaced by the difference of two integrals, the first extending from zero to infinity and the second from zero to r. Thus one obtains

$$D_W = 2\pi \int_0^\infty (\rho_o u_o^2 y\,dy - \rho u^2 \eta\,d\eta)$$

When the continuity relation between the two control surfaces

$$2\pi\rho_o u_o y\,dy = 2\pi\rho u\eta\,d\eta$$

is applied, the drag equation becomes

$$D_W = 2\pi\rho_o u_o^2 \int_0^\infty \left(1 - \frac{u}{u_o}\right) y\,dy$$

and the drag coefficient is given by

$$C_{D_W} = \frac{D_W}{q_o A} = \frac{2D_W}{\rho_o u_o^2 \pi r^2} = 4 \int_0^\infty \left(1 - \frac{u}{u_o}\right) \frac{y}{r}\, d\left(\frac{y}{r}\right) \tag{A2}$$

By means of the energy equation

$$(u/u_o)^2 = 1 + \left[2/(\gamma-1) M_o^2\right]\left[1 - (T/T_o)\right]$$

and the entropy relation

$$\Delta s = c_p \ln \frac{T}{T_o} - R\ln \frac{p}{p_o}$$

(where T/T_o and p/p_o are static temperature and pressure ratios, respectively, across the head shock wave)

or

$$\frac{T}{T_o} = e^{\frac{\Delta s}{c_p}} = \left(\frac{H_o}{H}\right)^{\frac{\gamma-1}{\gamma}} = \left[\frac{2\gamma M_o^2 \sin^2\theta - (\gamma-1)}{\gamma+1}\right]^{\frac{1}{\gamma}} \left[\frac{(\gamma-1)M_o^2\sin^2\theta +2}{(\gamma+1)M_o^2\sin^2\theta}\right]$$

equation (A2) can be written as

$$C_{D_W} = 4\int_0^\infty \left[1 - \sqrt{1 + \frac{2}{(\gamma-1)M_o^2}\left\{1 - \left[\frac{2\gamma M_o^2\sin^2\theta - (\gamma-1)}{\gamma+1}\right]^{\frac{1}{\gamma}}\left[\frac{(\gamma-1)M_o^2\sin^2\theta+2}{(\gamma+1)M_o^2\sin^2\theta}\right]\right\}}\,\right] \frac{y}{r}\, d\left(\frac{y}{r}\right)$$

$$\tag{A3}$$

where θ is the local shock wave angle (see fig. 13), T_O and H_O are free stream total (stagnation) temperature and pressure, respectively, and T and H correspond to conditions immediately downstream of the wave.

From a photograph of the flow about a body at a known Mach number, the values of wave angle θ can be tabulated for corresponding (y/r) distances, and the drag obtained by graphical integration of equation (A3).

Method 2: The method of integration of the entropy rise across the bow shock wave was proposed in reference 17 (equation (68)), from which the following expression is readily obtained:

$$C_{D_W} = \frac{4}{\gamma M_O^2} \int_0^\infty \ln\left(\frac{H_O}{H}\right) \frac{y}{r} \, d\left(\frac{y}{r}\right) \tag{A4}$$

This equation can be transformed by use of the energy and entropy relations into

$$C_{D_W} = \frac{4}{\gamma M_O^2} \int_0^\infty \ln\left\{\left[\frac{2\gamma M_O^2 \sin^2\theta - (\gamma-1)}{\gamma+1}\right]^{\frac{1}{\gamma-1}} \right.$$
$$\left[\frac{(\gamma-1)M_O^2 \sin^2\theta + 2}{(\gamma+1)M_O^2 \sin^2\theta}\right]^{\frac{\gamma}{\gamma-1}} \left.\right\} \frac{y}{r} \, d\left(\frac{y}{r}\right) \tag{A5}$$

Equations (A3) and (A5) are equivalent expressions for the wave drag.

Method 3: The determination of the body surface pressure distribution by the method of characteristics has been explained and used in references 4 and 16. Although very laborious, this method requires a picture of the shock wave only extensive enough to complete the characteristics net to the body surface. With such a photograph, this method is more accurate than the first two.

Of the three methods, the first two have presupposed a picture of the entire shock wave, or at least that portion of the wave across which the entropy changes significantly. In practice, however, such an extensive picture of a shock wave is generally unobtainable. An approximation is therefore required to account for the drag contribution of the unavailable portion of the wave.

References 18 and 19 suggest a method for finding the pressure drag due to the portion of the head shock wave bordering the subsonic region at the nose of a blunt body. This method approximates the head shock

wave by a hyperbola asymptotic to a free-stream Mach wave. In order to
determine if a close estimate of drag due to a complete head shock wave
could be obtained through this method by extrapolation of the hyperbola
to infinity, the head wave drag of a sphere at three Mach numbers was
computed. The results shown in figure 14 indicate poor agreement with
measurements of the actual fore drag of spheres. The discrepancy is
probably due to the fact that a hyperbola approximates the shape of the
shock wave well enough only in the section bordering the subsonic region,
while the shape of the outer part of the shock wave depends largely on
the shape of the body. Since in the case of a sphere the shock-wave
curvature changes continuously, the use of a hyperbola to obtain the
entire pressure drag seemed reasonable. The curvature of a shock wave
produced by a diffuser with a subsonic entrance usually does not change
continuously all along its length; therefore the application of a hyper-
bolic curve is invalid for determination of drag due to a complete wave.

An approximation, outlined in reference 16, is valuable since it
obviates need for knowledge of the outermost portion of the wave or the
construction of the characteristics net. Again referring to figure 13,
for the flow through a control plane HA, within the streamtube bounded
by the streamlines HGF and ABCDE, the continuity equation states

$$2\pi\rho_0 u_0 y\,dy = 2\pi\rho u\eta\,d\eta$$

or

$$\rho_0 u_0\,d\left(y^2\right) = \rho u\,d\left(\eta^2\right)$$

therefore

$$\eta^2 = \int_0^{y^2} \left(\frac{\rho_0}{\rho}\right)\left(\frac{u_0}{u}\right)d\left(y^2\right) + r^2$$

(since $\eta = r$ when $y = 0$)

With u_0/u given above by the energy equation, and

$$\frac{\rho_0}{\rho} = \frac{T}{T_0} = \left(\frac{H_0}{H}\right)^{\frac{\gamma-1}{\gamma}}$$

it follows that

$$\eta^2 = \int_0^{y^2} \frac{\left(\dfrac{H_0}{H}\right)^{\frac{\gamma-1}{\gamma}}}{\sqrt{1 + \dfrac{2}{(\gamma-1)M_0^2}\left[1 - \left(\dfrac{H_0}{H}\right)^{\frac{\gamma-1}{\gamma}}\right]}}\,d\left(y^2\right) + r^2$$

or

$$\left(\frac{\eta}{r}\right)^2 - \left(\frac{y}{r}\right)^2 = \int_0^{\frac{y^2}{r^2}} \left\{ \frac{\left(\frac{H_o}{H}\right)^{\frac{\gamma-1}{\gamma}}}{\sqrt{1 + \frac{2}{(\gamma-1)M_o^2}\left[1 - \left(\frac{H_o}{H}\right)^{\frac{\gamma-1}{\gamma}}\right]}} - 1 \right\} d\left(\frac{y}{r}\right)^2 + 1 \tag{A6}$$

where

$$\left(\frac{H_o}{H}\right)^{\frac{\gamma-1}{\gamma}} = \left[\frac{2\gamma M_o^2 \sin^2\theta - (\gamma-1)}{\gamma+1}\right]^{\frac{1}{\gamma}} \left[\frac{(\gamma-1)M_o^2\sin^2\theta + 2}{(\gamma+1)M_o^2\sin^2\theta}\right]$$

Now, writing the summation of forces for the region HABCDEFGH, one obtains

$$C_{D_W} = \left(C_{D_W}\right)_o + \frac{p-p_o}{q_o}\left[\frac{\pi(\eta^2-y^2)}{\pi r^2}\right] = \left(C_{D_W}\right)_o + \frac{p-p_o}{\frac{1}{2}\gamma p_o M_o^2}\left[\left(\frac{\eta}{r}\right)^2 - \left(\frac{y}{r}\right)^2\right]$$

or

$$C_{D_W} = \left(C_{D_W}\right)_o + \frac{2(K-1)}{\gamma M_o^2}\left[\left(\frac{\eta}{r}\right)^2 - \left(\frac{y}{r}\right)^2\right] \tag{A7}$$

where

$$K = \left(\frac{p}{p_o}\right)_{GF}$$

where $\left(C_{D_W}\right)_o$ is the drag coefficient obtained by use of equation (A3) or (A5) for the region between B and G. Point G is assumed to be the last visible point on the shock-wave photograph, and K is the ratio of the static pressure at some point along the streamline from point G to point F to p_o.

The value of K is known only at the points G and F along the streamline, being given at point G by the equation for the pressure rise through an oblique shock wave

$$\left(\frac{p}{p_o}\right)_G = \left[\frac{2\gamma M_o^2 \sin^2\theta - (\gamma-1)}{\gamma+1}\right]_G$$

and equal to unity at point F. Hence the average pressure ratio K lies between $(p/p_0)_G$ and 1.0. The choice of $K = (p/p_0)_G$ generally results in an overestimated drag coefficient, while the choice of $K = \frac{1}{2}\left[1+(p/p_0)_G\right]$ generally yields an underestimated value of C_{D_w}. The fraction of the total drag taken into account by the approximation should be small if good accuracy is desirable. Thus the value of $(C_{D_w})_0$ must be calculated for a maximum span of the bow wave for best accuracy.

Before applying the above methods to the calculation of the drag of diffusers, it was decided to test the procedure on spheres, for which an experimental fore-drag curve and excellent wave photographs were available. Figure 14 shows the experimental data from reference 20 and the calculated values of drag. It is evident that the portions of the head shock waves contained in the photographs from which the wave drag was calculated were insufficient for accurate determination of the drag coefficients. Since the photographs showed the wave shapes up to 15 sphere radii from the axis of symmetry, it may be concluded that the visible part of the wave must be definitely in excess of this figure. The indicated differences between the drag coefficients calculated by the momentum method (equation (A3)) and the entropy method (equation (A5)) are due solely to inaccuracies in calculations and mechanical integrations. The approximation outlined in reference 16, when applied to the drag curve of figure 14 as calculated by the momentum method, yields a much better estimate of the drag coefficients. However, to obtain this agreement it was necessary to use for K the full value of pressure ratio across the oblique shock wave at the extreme y/r visible on the photograph.

Application of the method of characteristics, as outlined in reference 4, to the flow around a 1-inch-diameter sphere at a Mach number of 3, proved unsuccessful. The characteristics net could not be completed from the shock wave to the sphere because of extremely slow convergence of the Mach net toward the sphere. The schlieren photographs of spheres used for drag calculations were taken in the Ames 1- by 3-foot supersonic wind tunnels No. 1 and No. 2.

ADDITIONAL CONSIDERATIONS

The experience of calculating drag from wave photographs led to a few observations which may aid in future work:

1. The photograph of the wave must be clear, accurate, and extensive, in excess of 15 maximum body radii if possible. Shadowgraph

pictures are preferable to schlieren photographs because of better def-
inition of the head-wave curvature near the leading edges of cowlings;
a small error in the apparent curvature of the wave immediately adjacent
to the lip of a cowling of small angle may result in a large error in
the calculated drag.

2. The free-stream Mach number must be accurately known (for a
sphere at $M_O = 1.520 \pm 0.004$, $\Delta C_{D_W} = \pm 0.01$).

3. The position of the body should be such that the head wave it
creates does not intersect any other pressure disturbances which may be
present in the tunnel (e.g., shock or expansion waves created by tunnel-
wall imperfections, model support, etc.).

4. The methods are not applicable to the calculation of drag of a
body the cross-section of which continually increases within the field
of view. In this case, a large portion of the drag would have to be
estimated by means of the approximation suggested by Nucci, and the
error in calculated drag coefficient would be large.

5. A body of revolution may yaw slightly without disturbing the
symmetry of the detached head shock wave; consequently, the wave axis of
symmetry rather than the body axis should be used as the x axis. The
calculated drag coefficient must be resolved in such cases in the direc-
tion of the body axis to obtain the axial-force coefficient.

REFERENCES

1. Brown, Clinton E., and Parker, Hermon M.: A Method for the
    Calculation of External Lift, Moment, and Pressure Drag of
    Slender Open-Nose Bodies of Revolution at Supersonic Speeds.
    NACA Rep. 808, 1945.

2. Ferri, Antonio: Application of the Method of Characteristics to
    Supersonic Rotational Flow. NACA Rep. 841, 1946.

3. Munk, Max M., and Crown, J. Conrad: The Head Shock Wave. Naval
    Ord. Lab. Memo. No. 9773, Aug. 25, 1948.

4. Ferri, Antonio: Method for Evaluating from Shadow or Schlieren
    Photographs the Pressure Drag in Two-Dimensional or Axially
    Symmetrical Flow Phenomena with Detached Shock. NACA TN 1808,
    1949.

5. Prandtl, L.: The Mechanics of Viscous Fluids. Aerodynamic Theory,
    vol. III, by Durand, W. F., California Inst. of Technology,
    Pasadena, 1943.

6. Schlichting, H.: Lecture Series, "Boundary Layer Theory," Pt. I —
    Laminar Flows. NACA TM 1217, 1949. Pt. II — Turbulent Flows.
    NACA TM 1218, 1949.

7. Frankl, F., and Voishel, V.: Turbulent Friction in the Boundary
    Layer of a Flat Plate in a Two-Dimensional Compressible Flow at
    High Speeds. NACA TM 1053, 1943.

8. von Kármán, T., and Tsien, H. S.: Boundary Layer in Compressible
    Fluids. Jour. Aero. Sci., vol. 5, no. 6, 1938, p. 227.

9. Oswatitsch, K.: Pressure Recovery for Missiles With Reaction
    Propulsion at High Supersonic Speeds (The Efficiency of Shock
    Diffusers). NACA TM 1140, 1947.

10. Davis, Wallace F., Brajnikoff, George B., Goldstein, David L., and
    Spiegel, Joseph M.: An Experimental Investigation at Supersonic
    Speeds of Annular Duct Inlets Situated in a Region of Appreciable
    Boundary Layer. NACA RM A7G15, 1947.

11. Massachusetts Institute of Technology, Dept. of Elec. Engr. Center
    of Analysis: Tables of Supersonic Flow Around Cones, by Staff
    of Computing Section, Center of Analysis, under direction of
    Zdeněk Kopal, MIT Tech. Rep. No. 1, Cambridge, Mass., 1947.

12. Mangler, W.: Compressible Boundary Layers on Bodies of Revolution. MAP, Völkenrode, Repts. and Trans. 47, Mar. 15, 1946.

13. Sibulkin, Merwin: Theoretical and Experimental Investigation of Additive Drag. NACA RM E51B13, 1951.

14. Pendley, Robert E., and Robinson, Harold L.: An Investigation of Several NACA 1-Series Nose Inlets With and Without Protruding Central Bodies at High Subsonic Mach Numbers and at a Mach Number of 1.2. NACA TN 3436, 1955.

15. Ferri, Antonio, and Nucci, Louis M.: The Origin of Aerodynamic Instability of Supersonic Inlets at Subcritical Conditions. NACA RM L50K30, 1950.

16. Nucci, Louis M.: The External-Shock Drag of Supersonic Inlets Having Subsonic Entrance Flow. NACA RM L50G14a, 1950.

17. Oswatitsch, K. C.: Flows of Compressible Fluids; Fundamental Notions and General Theorems. AVA Monographs, A. Betz, ed. MAP, Völkenrode, Repts. and Trans. 992, Mar. 15, 1948.

18. Moeckel, W. E.: Approximate Method for Predicting Form and Location of Detached Shock Waves Ahead of Plane or Axially Symmetric Bodies. NACA TN 1921, 1949.

19. Moeckel, W. E.: Experimental Investigation of Supersonic Flow With Detached Shock Waves for Mach Numbers Between 1.8 and 2.9. NACA RM E50D05, 1950.

20. Erdmann, S.: Widerstand und Stabilität von Geschosskörpern. Lilienthal - Gesellschaft für Luftfahrtforschung, Peenemunde, Germany, Bericht 139, Teil 2, Oct. 9-10, 1941, pp. 28-31.

1   Nose inlet model
2   Shroud
3   Floating shell supporting model
4   Stationary shell supporting shroud
5   Strain gage measuring drag force
6   Survey rake
7   Ring and plug for mass flow control
8   Locking screw used during model changes
9   Wedge for outlet area adjustment
10 Mechanism for rotating survey rake
11 Supporting struts
12 Holes for setting angle of attack
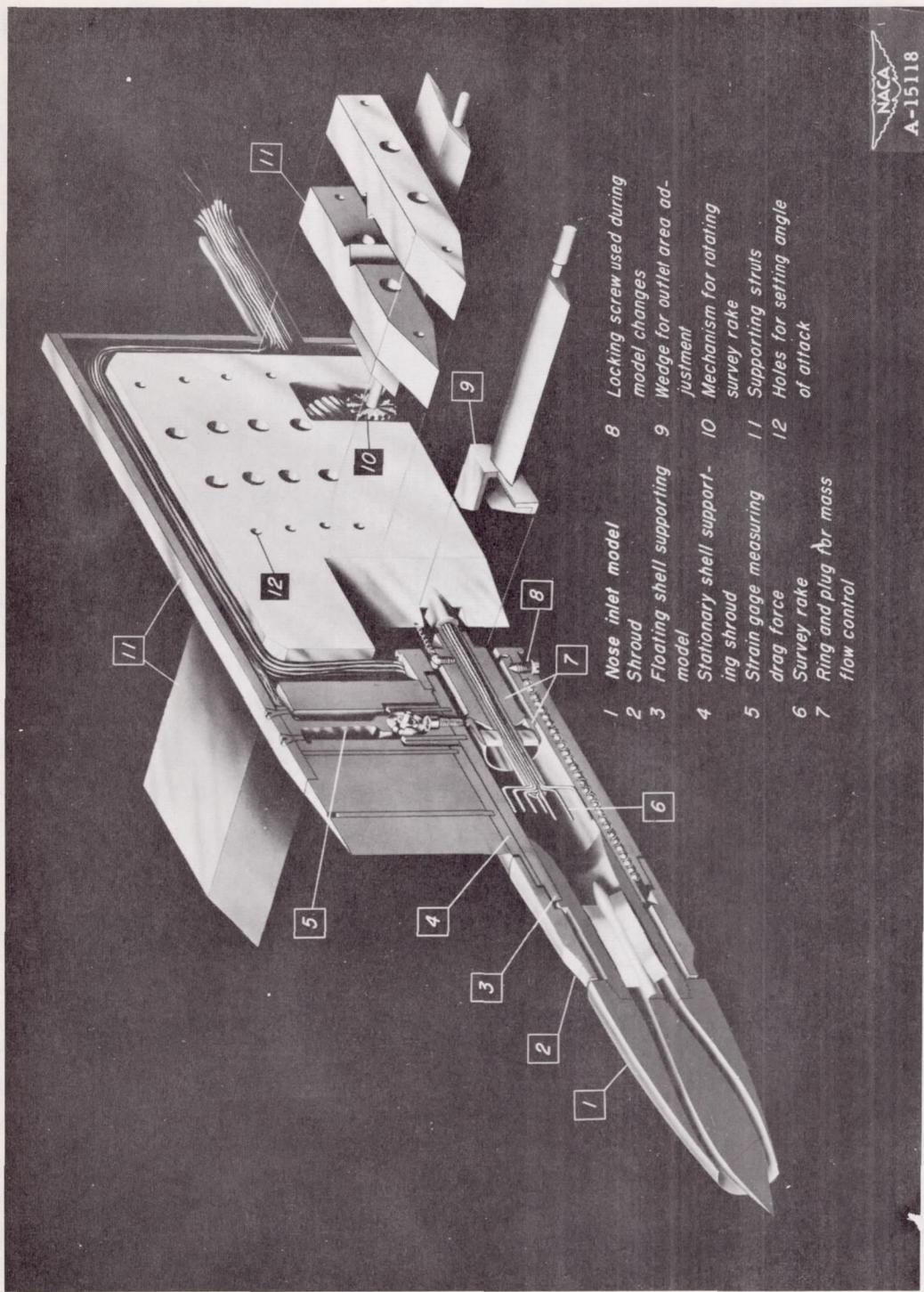
Figure 1.— Apparatus for measuring the performance of supersonic diffusers.

Station X	Orifices
0.550	1 & 5
1.350	2 & 6
2.050	3 & 7
2.700	4 & 8
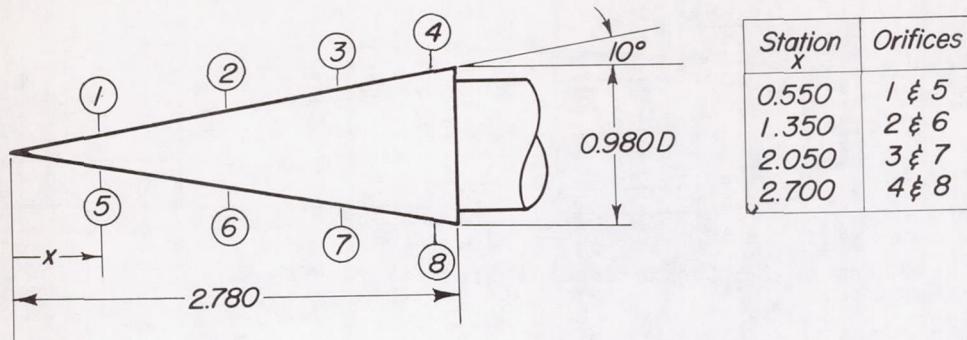
(a)   20° cone with 8 static-pressure orifices.
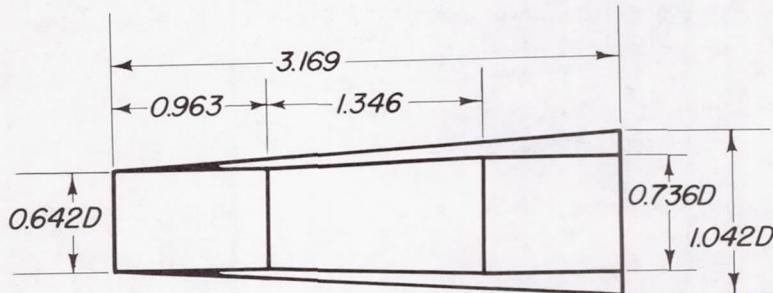
(b)   Model A.- Open-nose diffuser with a straight inlet section.
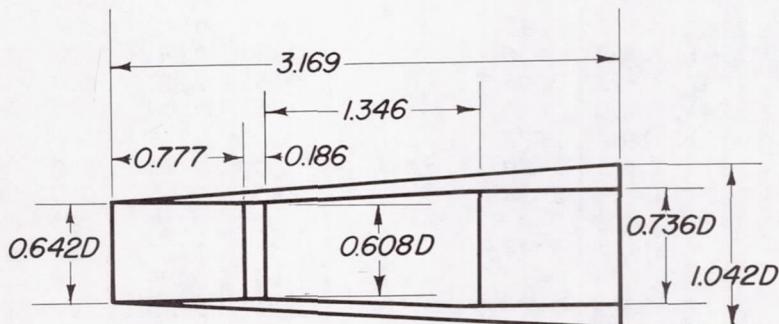
(c)   Model B.- Open-nose diffuser with contraction.

Note: All dimensions are given in inches.

Figure 2.— Model dimensions.
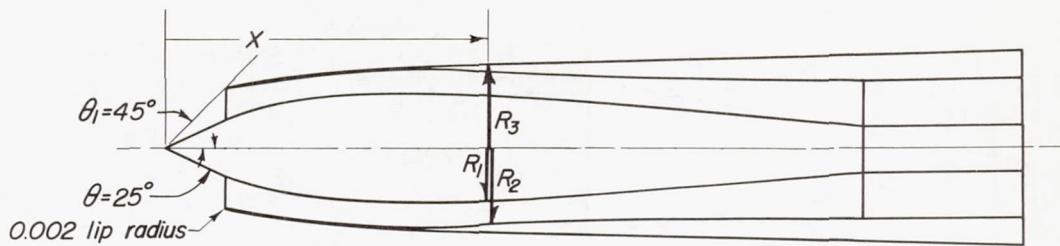
(d)   Model C.— Conical-shock diffuser with internal contraction.
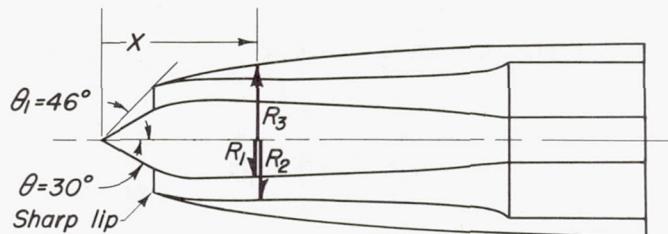
Note: All radii are given
normal to model axes.

All dimensions
are given in inches.

(e)   Model D.—Conical-shock diffuser
without internal contraction.

Model C ordinates

Station X	R_1	R_2	R_3
0	0	—	—
0.322	0.149	0.323	0.323
0.324	0.151	0.321	0.329
0.400	0.184	0.332	0.347
0.500	0.212	0.346	0.363
0.600	0.234	0.361	0.377
0.700	0.252	0.373	0.389
0.800	0.265	0.384	0.400
0.900	0.276	0.393	0.409
1.000	0.284	0.400	0.417
1.100	0.290	0.407	0.423
1.200	0.293	0.413	0.430
1.300	0.294	0.419	0.436
1.400	0.295	0.423	0.440
1.500	0.295	0.427	0.444
1.900	0.273	0.409	0.453
2.400	0.238	0.392	0.466
2.900	0.197	0.380	0.478
3.400	0.153	0.372	0.490
3.702	0.125	0.368	0.498
4.560	0.125	0.368	0.521

Model D ordinates

Station X	R_1	R_2	R_3
0	0	—	—
0.272	0.154	0.282	0.282
0.300	0.167	0.290	0.292
0.350	0.186	0.304	0.310
0.400	0.197	0.312	0.326
0.500	0.211	0.322	0.354
0.575	0.212	0.327	0.367
0.650	0.210	0.329	0.380
0.750	0.207	0.328	0.395
0.850	0.204	0.328	0.408
1.000	0.198	0.326	0.426
1.500	0.176	0.332	0.472
1.900	0.147	0.350	0.497
2.000	0.137	0.360	0.501
2.057	0.125	0.368	0.503
2.500	0.125	0.368	0.518
2.918	0.125	0.368	0.521

Figure 2.- Concluded.
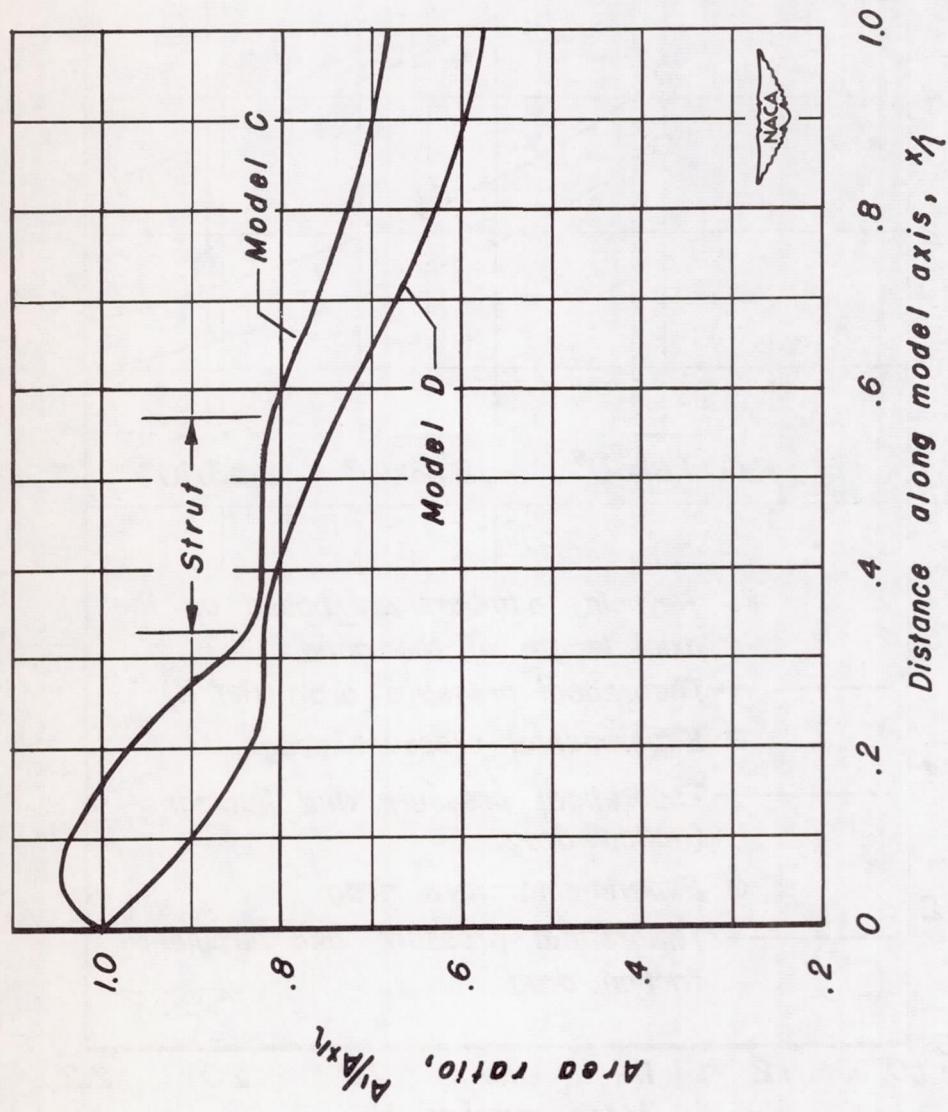
Figure 3.- Variation of diffuser area ratio normal to mean flow direction with diffuser length.
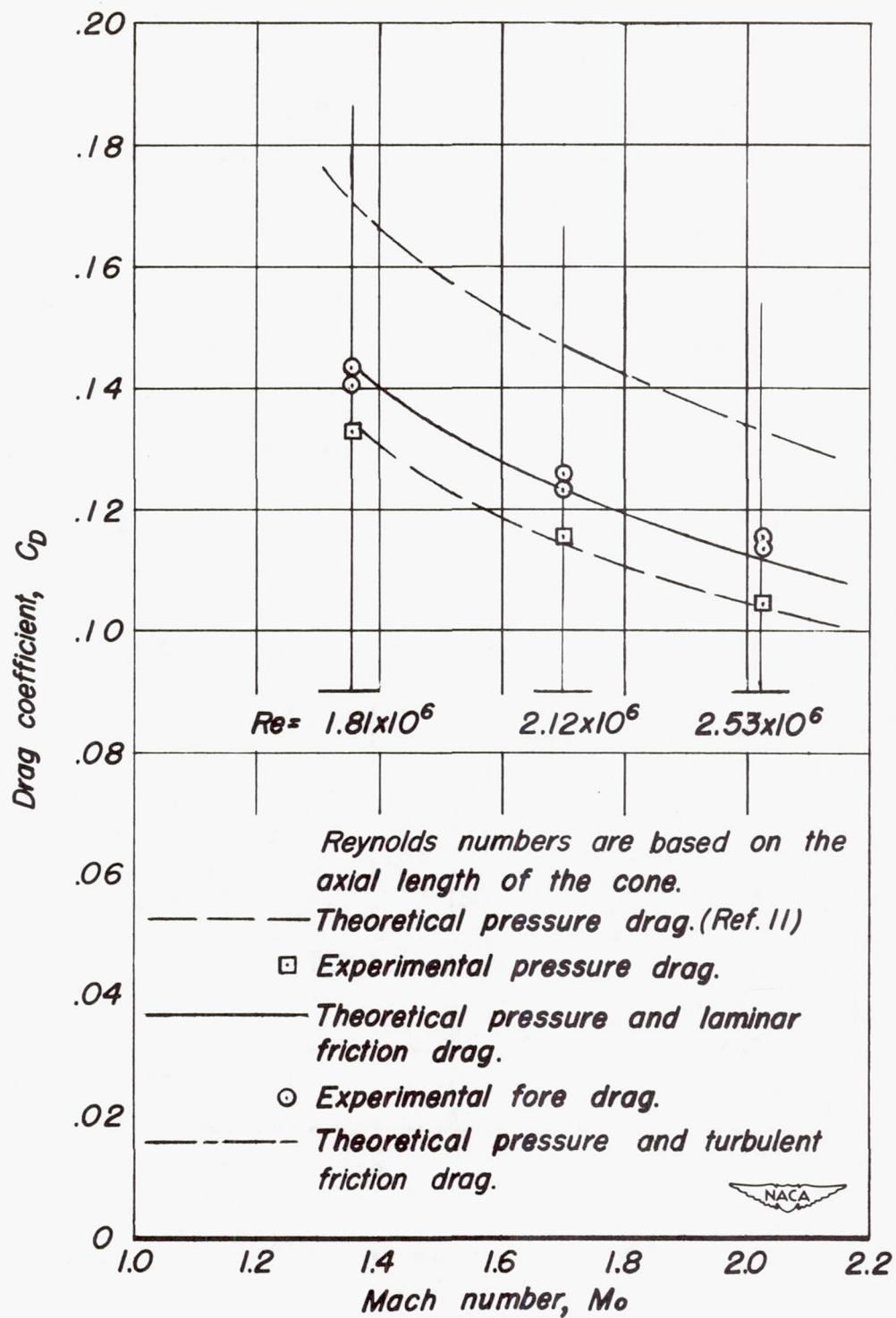
Figure 4.-Fore drag of a 10° semi-angle cone.
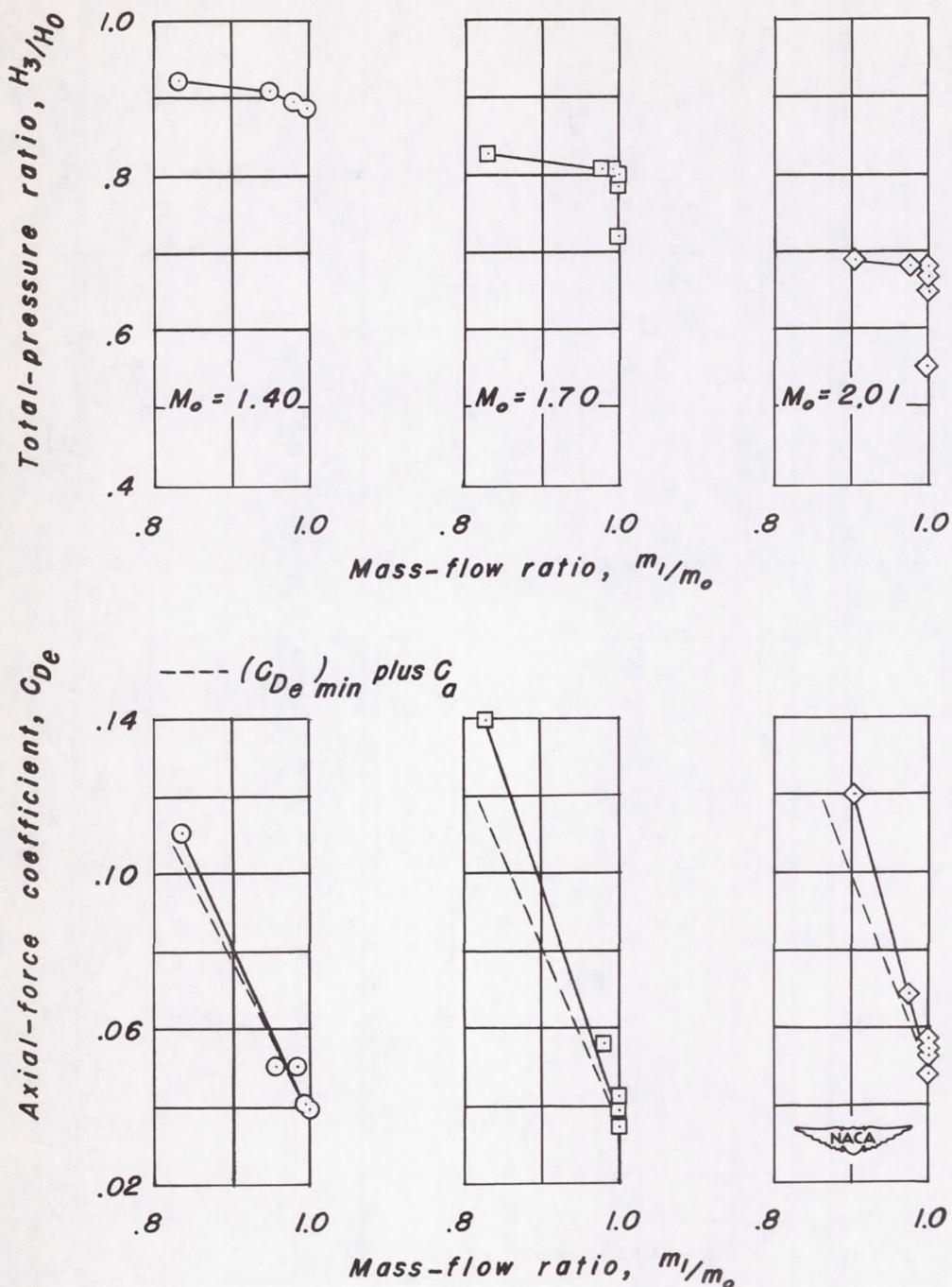
Figure 5.-Variation of total-pressure ratio and axial-force coefficient of model A with mass-flow ratio and Mach number at α = 0°.
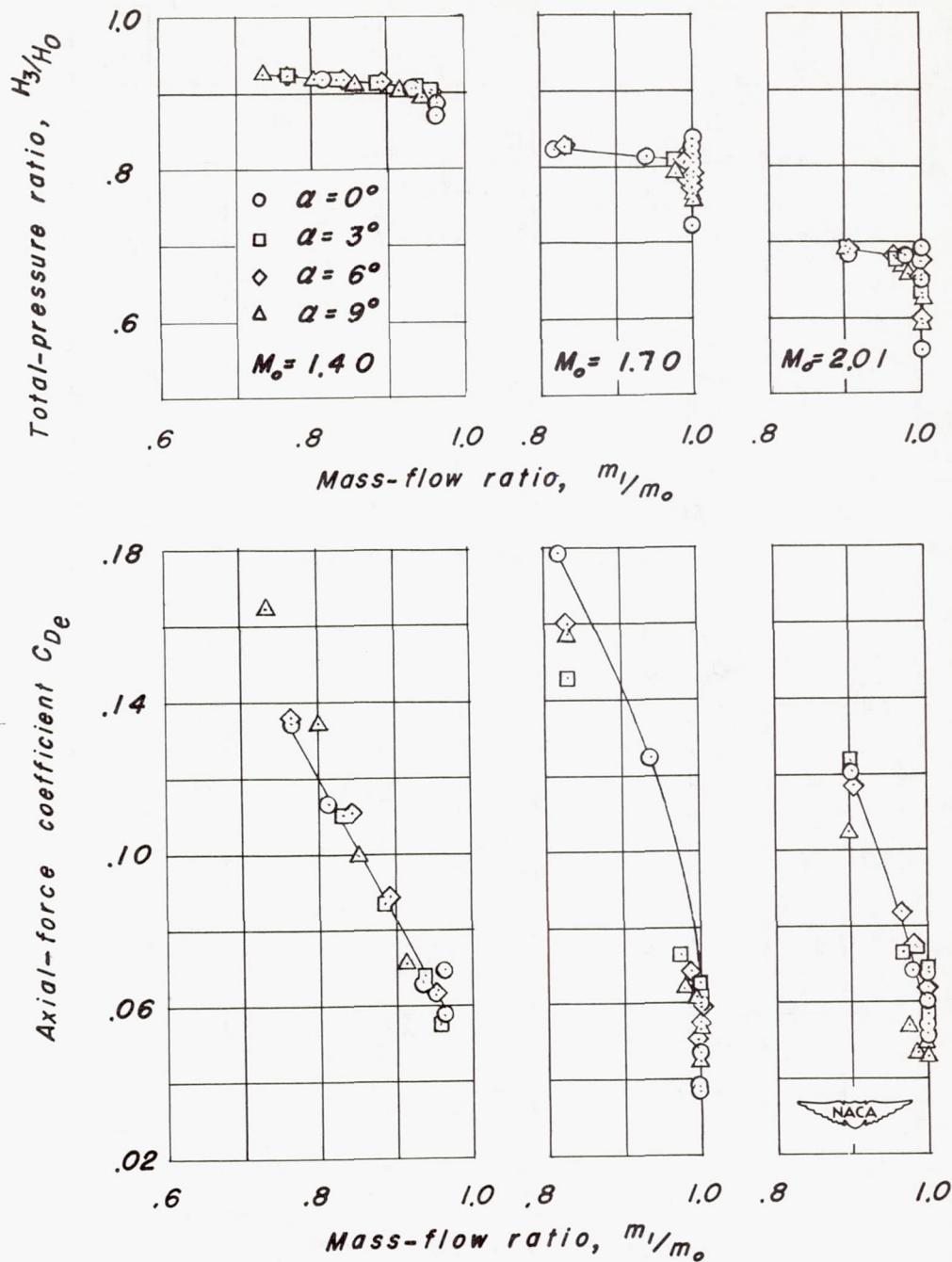
Figure 6.—Variation of total-pressure ratio and axial-
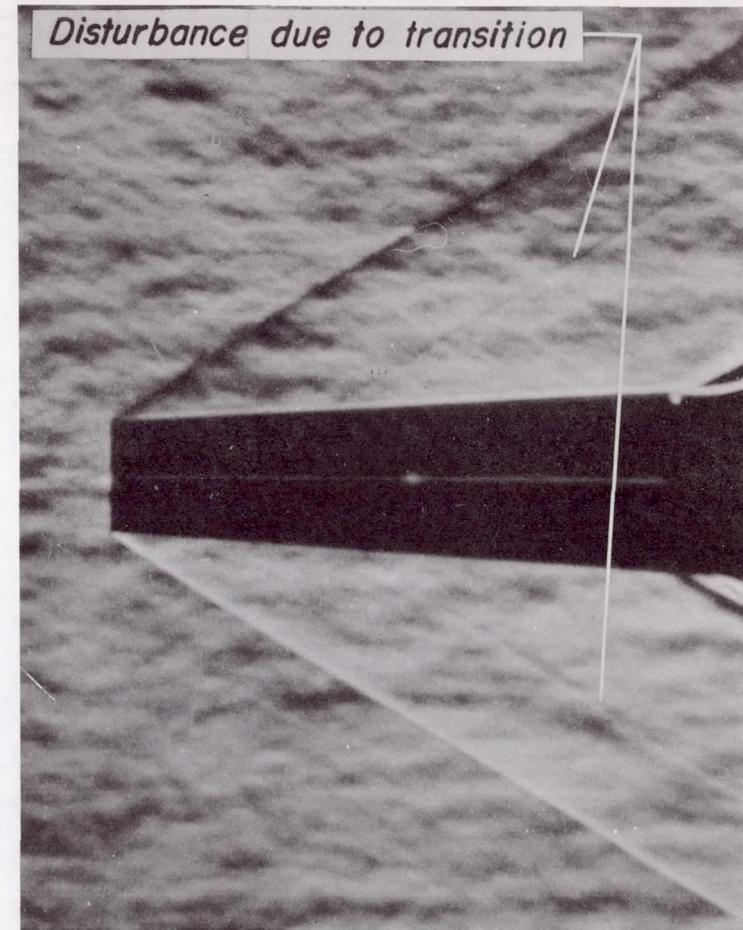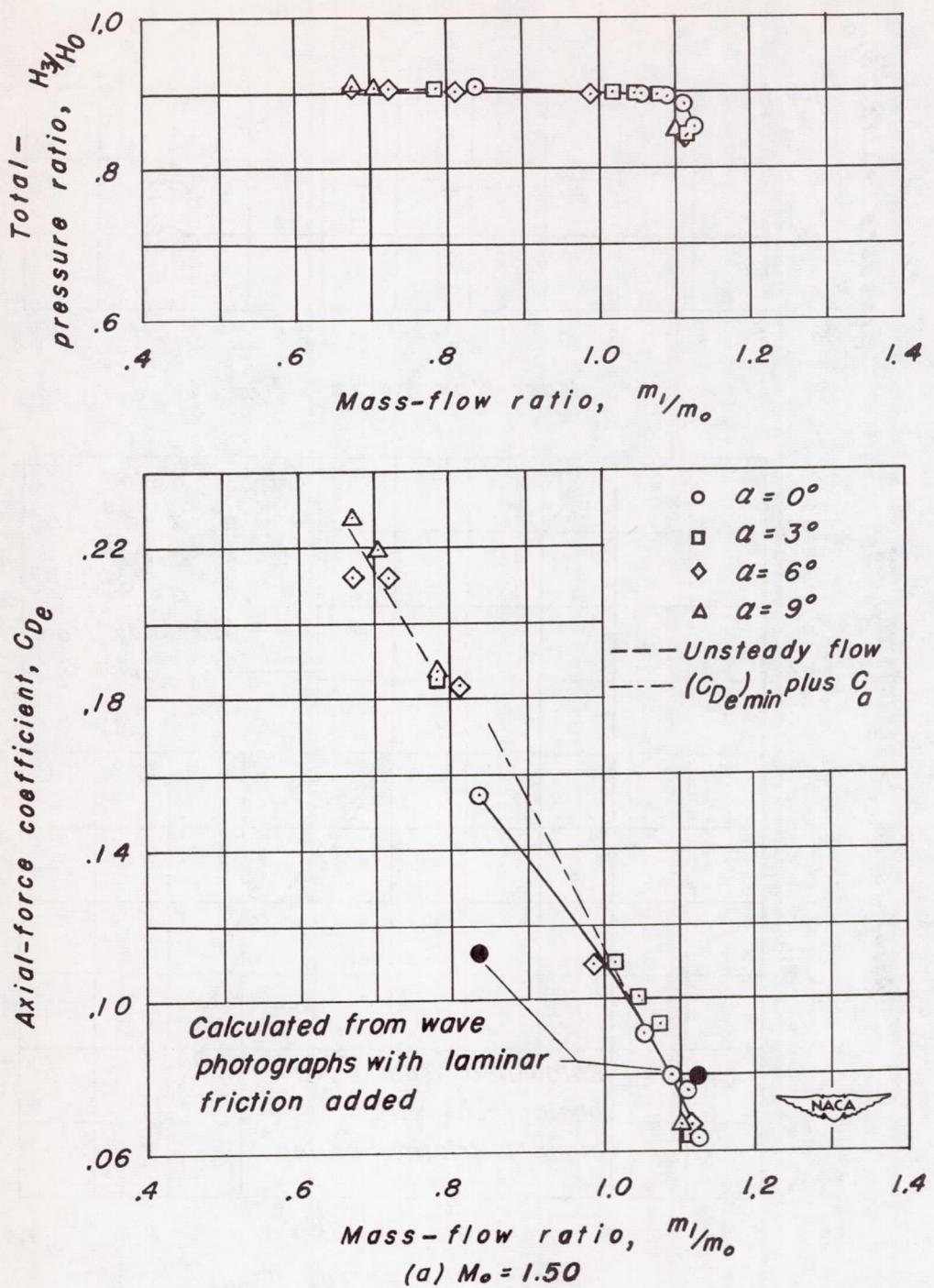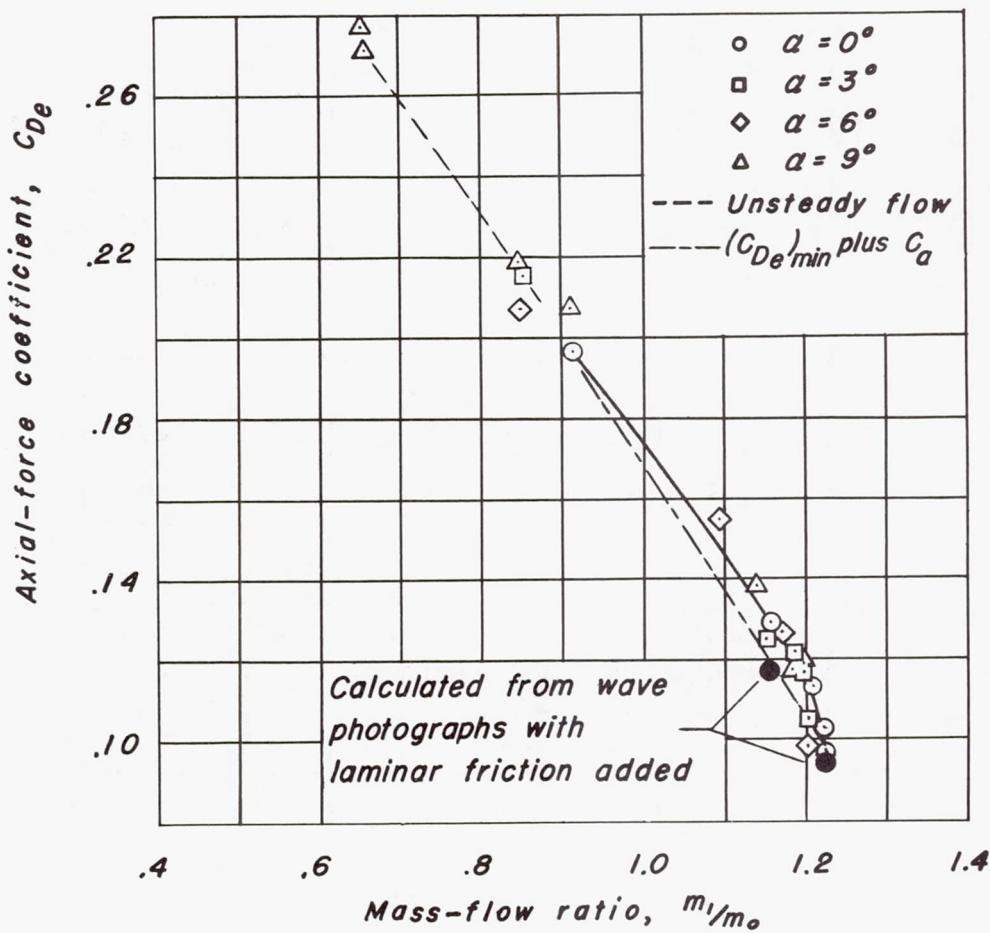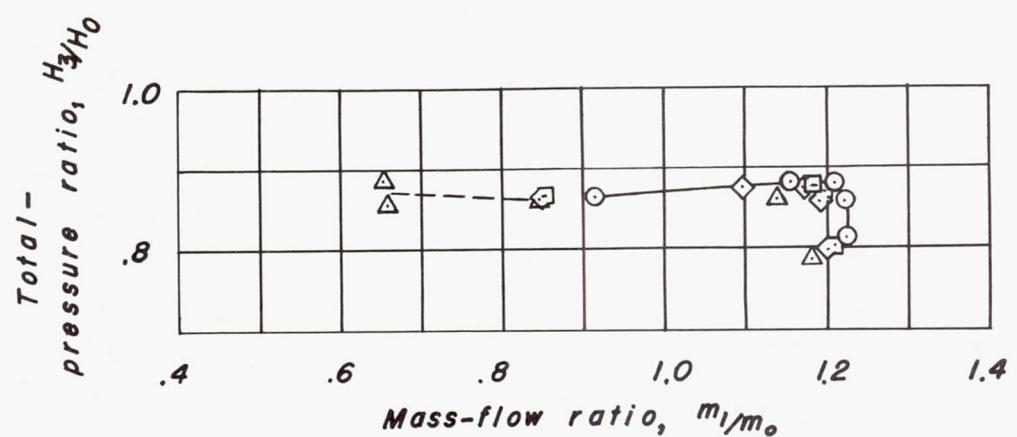force coefficient of model B with mass-flow ratio,
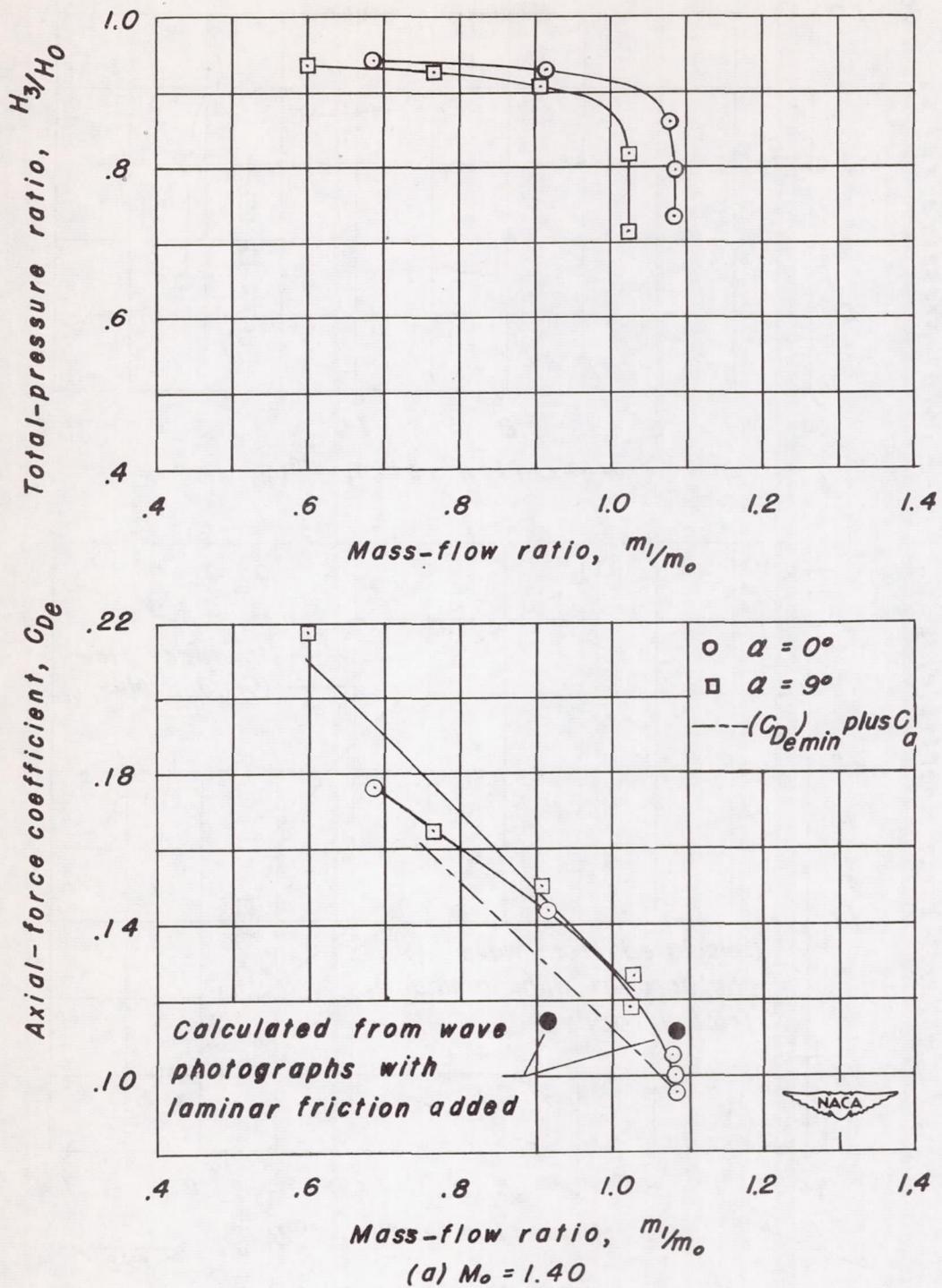angle of attack, and Mach number.
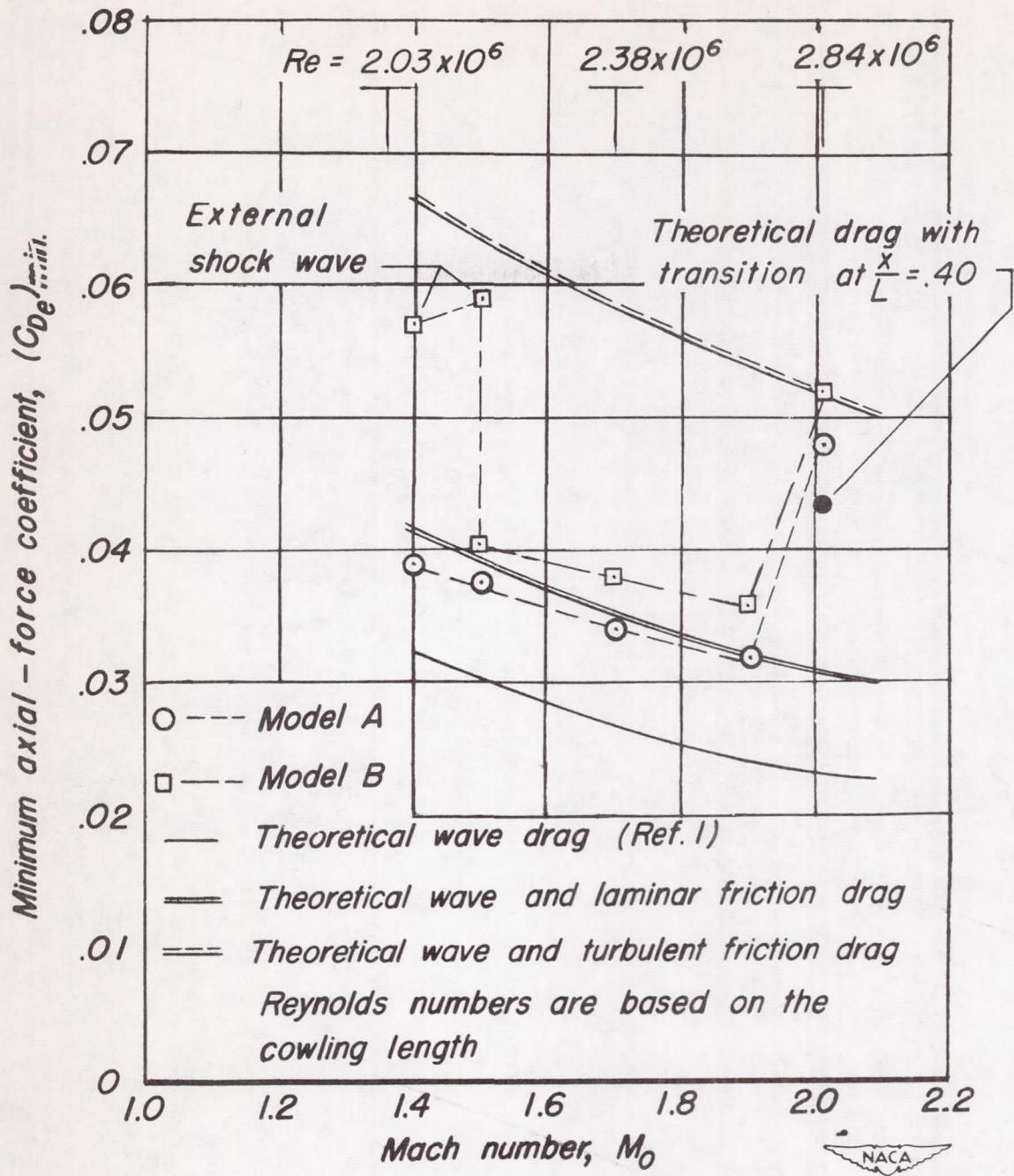
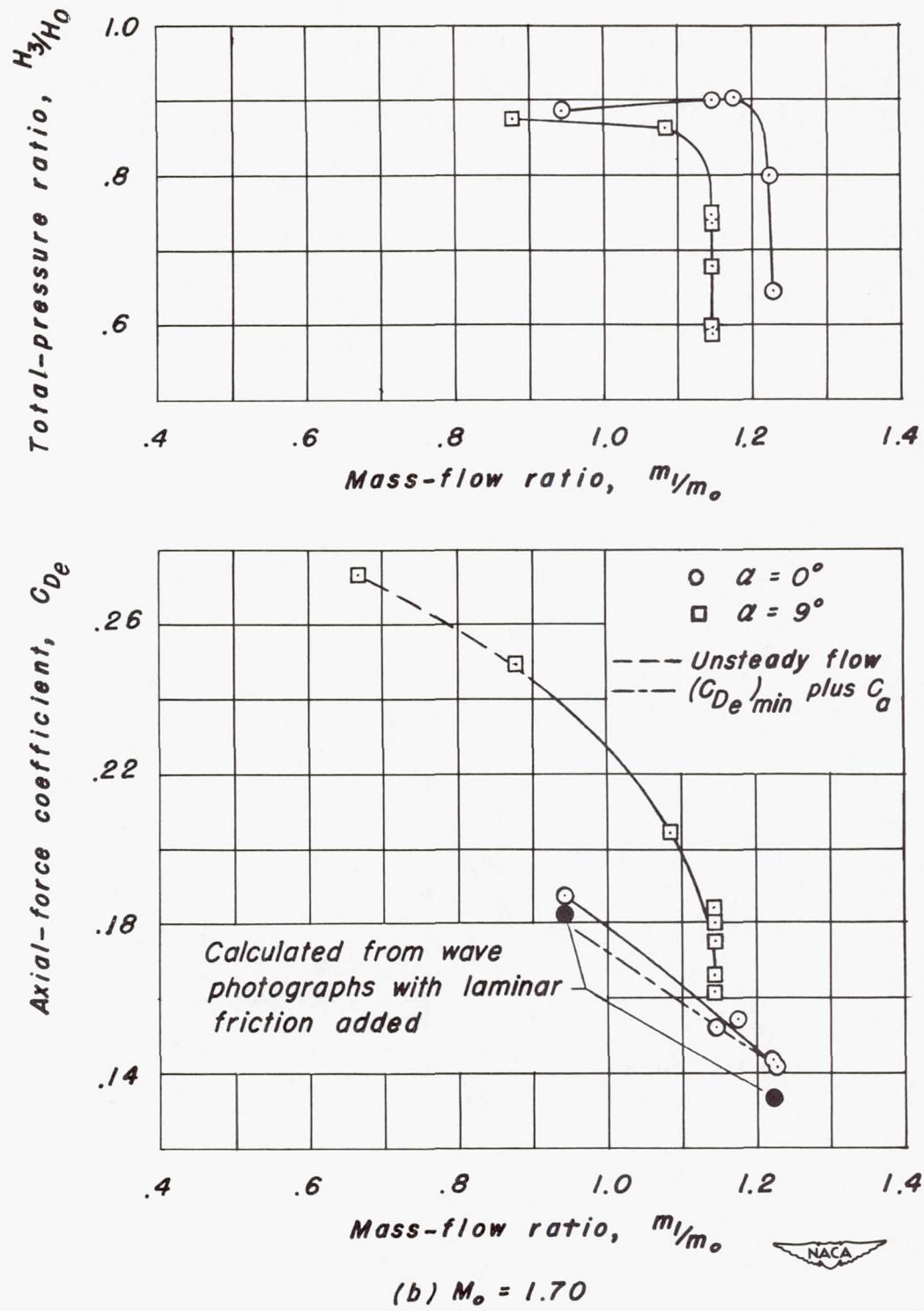Figure 7. - Variation of the minimum axial-force
    coefficient of models A and B with Mach number
    at $\alpha = 0°$.

Disturbance due to transition
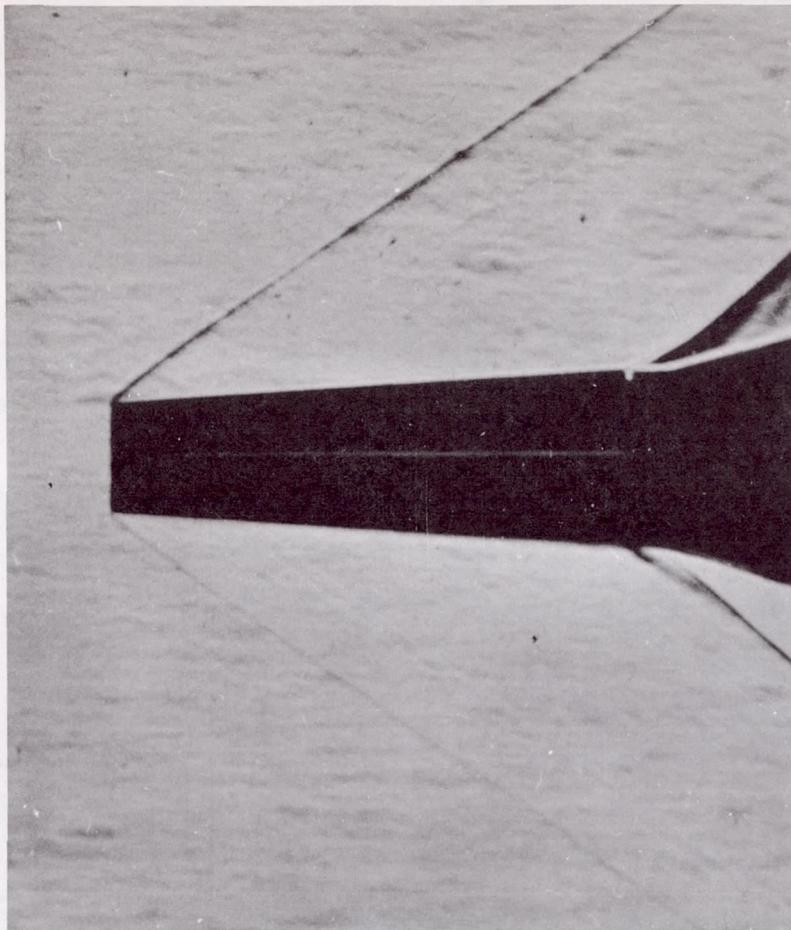
$M_O = 1.90$

$M_O = 2.01$

NACA
A-15694

Figure 8.— Typical schlieren photographs of model A showing the pressure distribution due to boundary—
layer transition at $M_O = 2.01$.

Figure 9.— Variation of total-pressure ratio and axial-
force coefficient of model C with mass-flow ratio
and angle of attack at various Mach numbers.

(b) $M_o = 1.70$

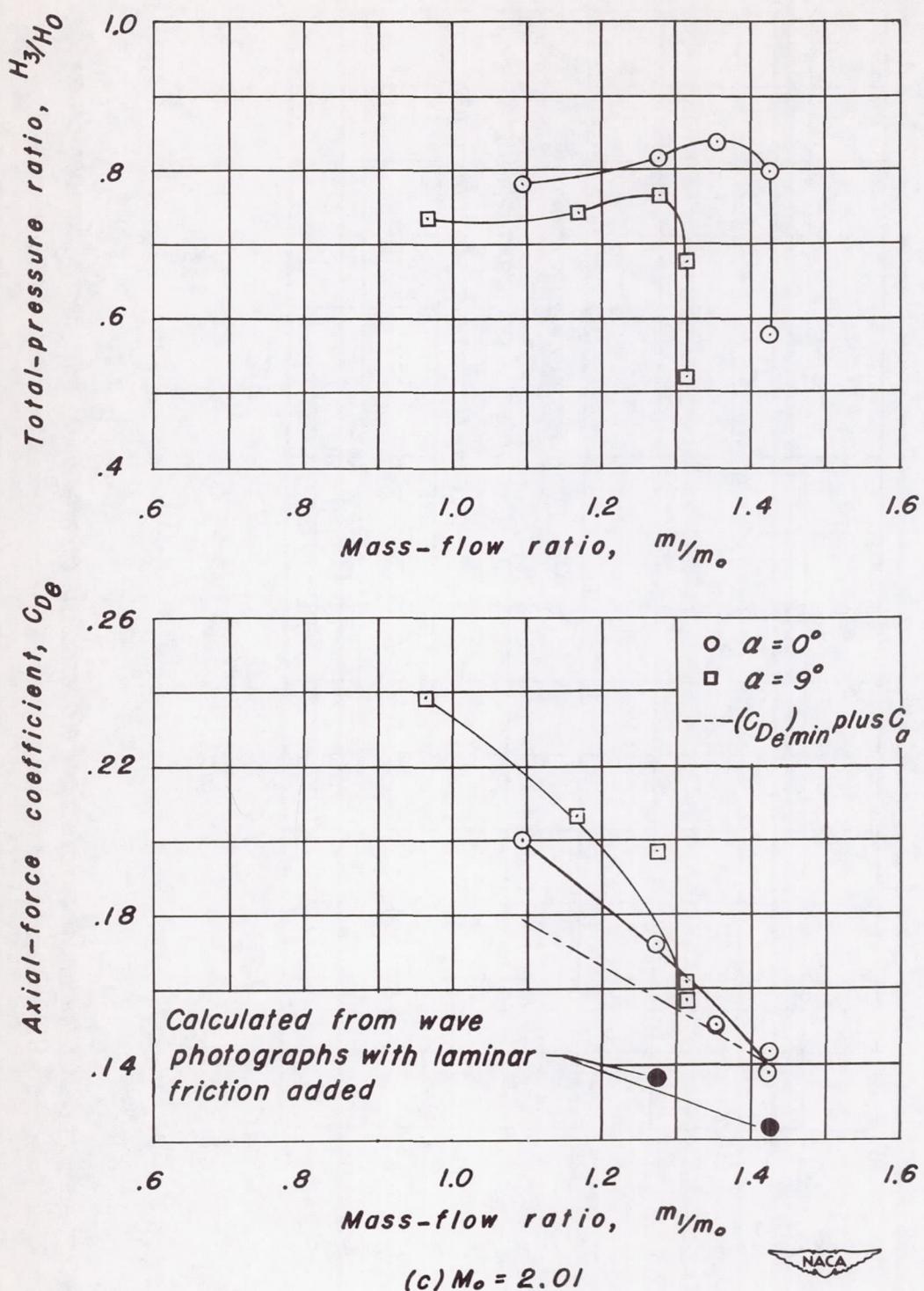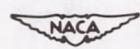Figure 9.— Continued.

(c) $M_o = 2.01$
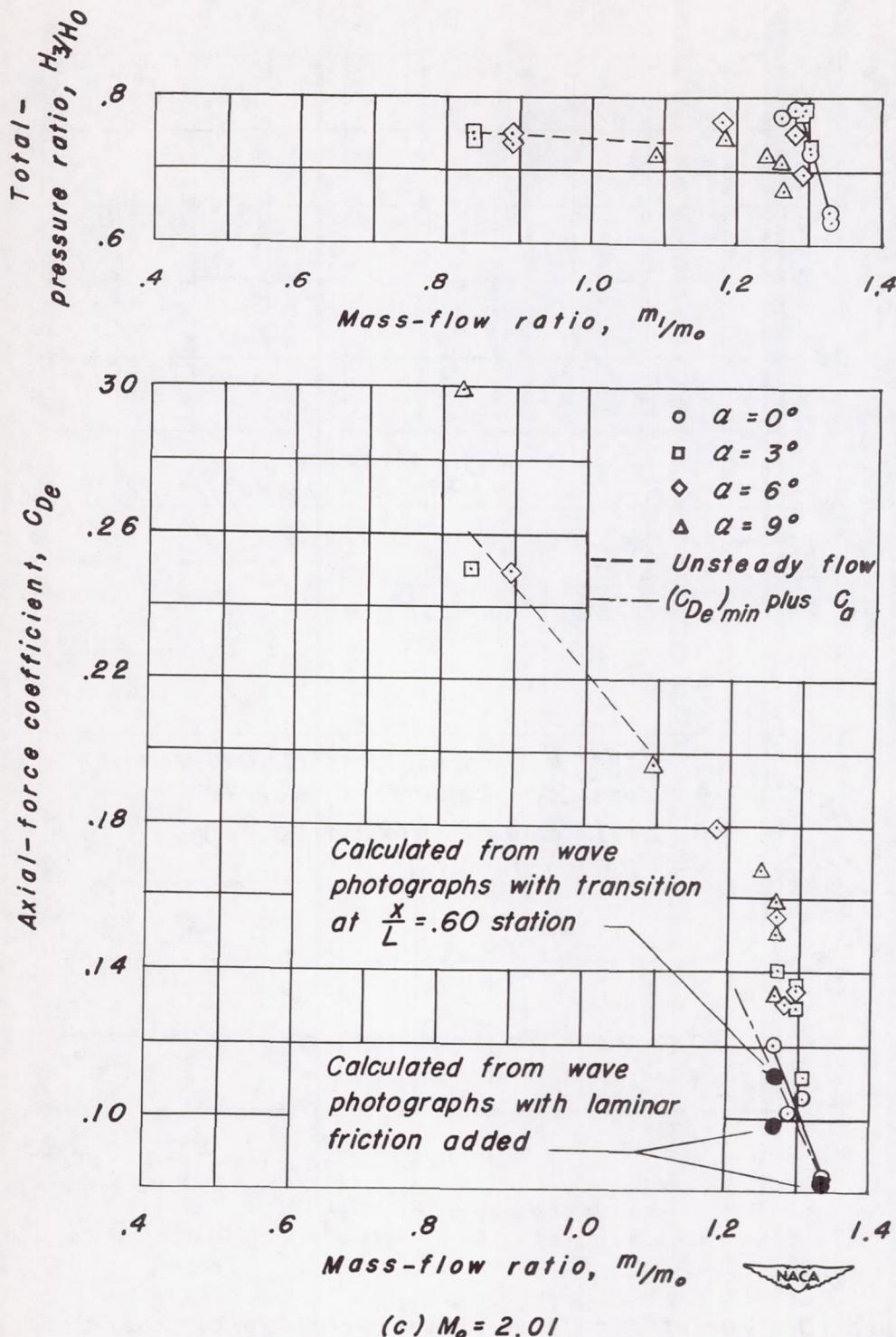
Figure 9.- Concluded.
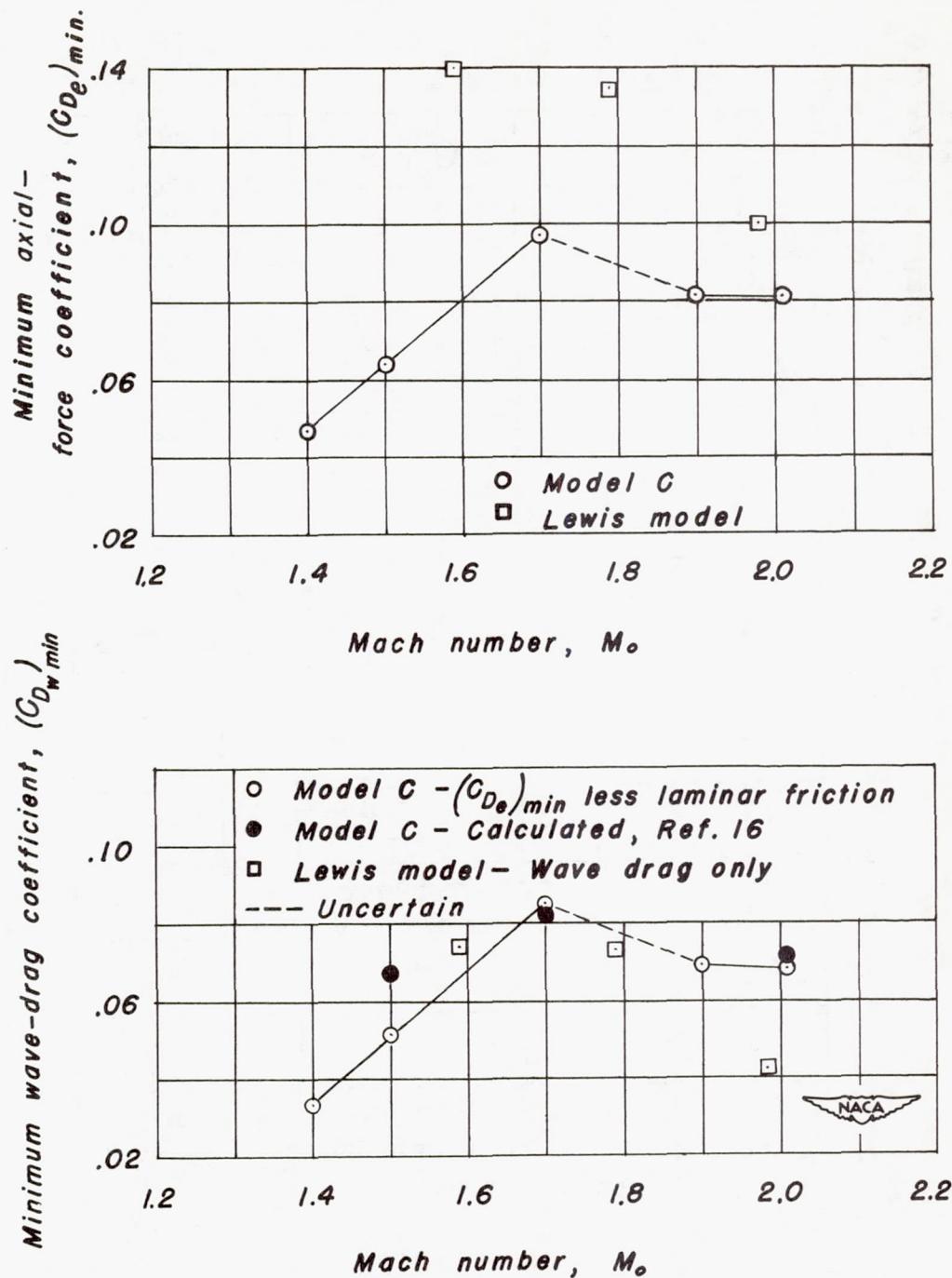
Figure 10.- Variations in minimum axial-force coefficients
of model C and Lewis model with Mach number at $\alpha = 0°$.

Figure 11.— Variation of total-pressure ratio and axial-force
coefficient of model D with mass-flow ratio and angle of attack
at various Mach numbers.

(b) $M_o = 1.70$

Figure 11.— Continued.

(c) $M_0 = 2.01$

Figure 11.- Concluded.
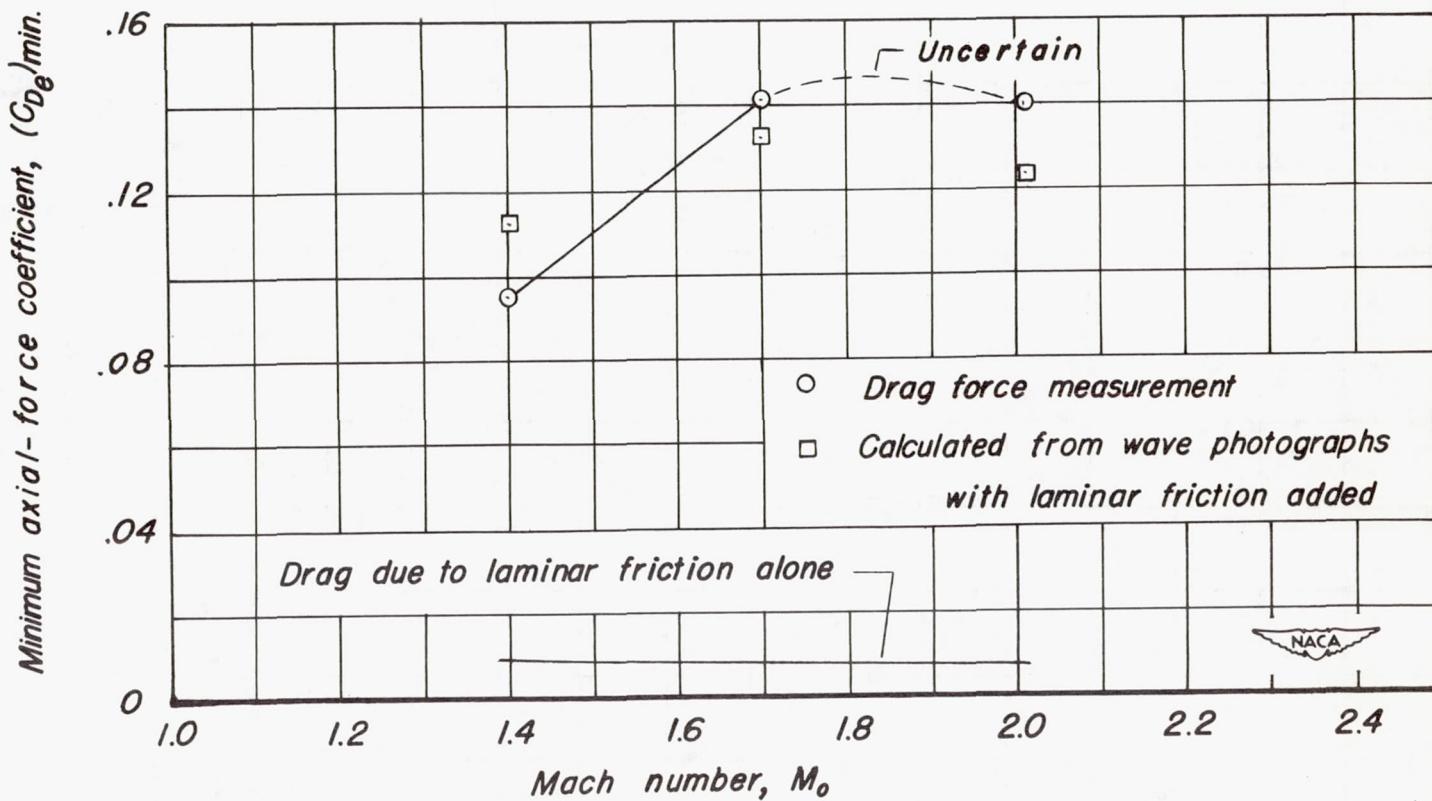
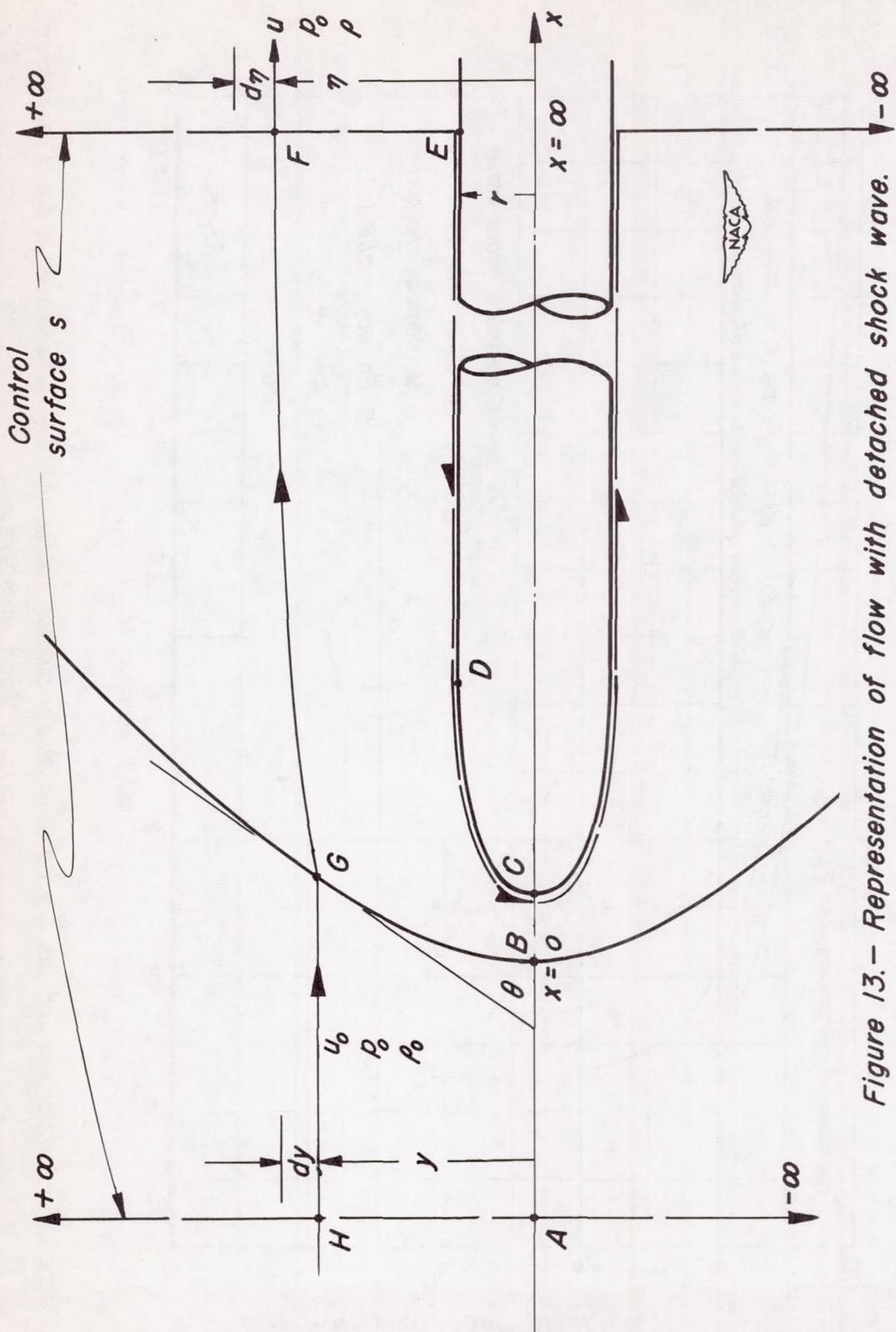Figure 12.—Variation of minimum axial-force coefficient of model D with Mach number at α=0°.

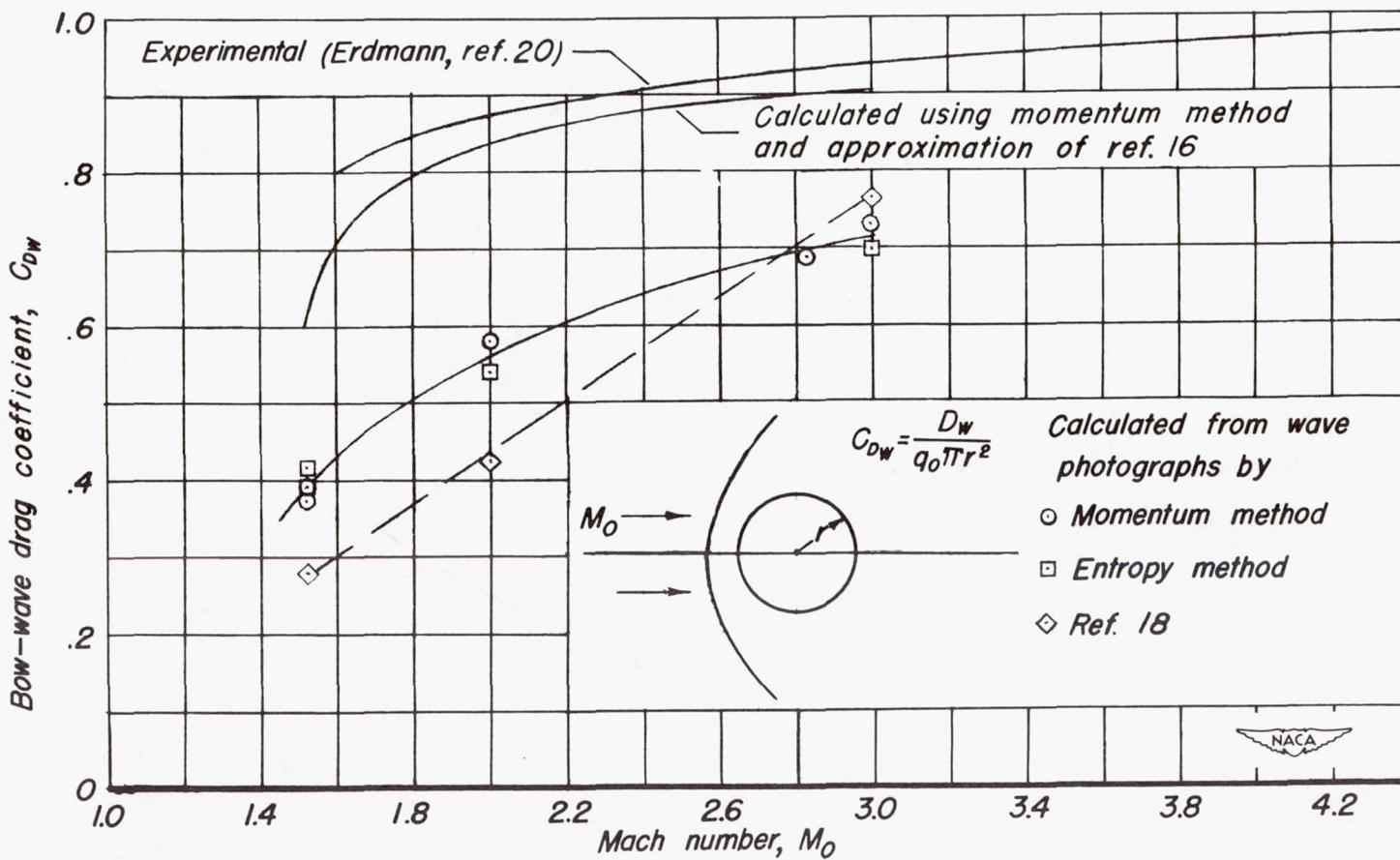Figure 13.— Representation of flow with detached shock wave.

Figure 14.–Comparison of calculated and experimental values of the bow-wave drag of a sphere at various Mach numbers.